Identification and Design Principles of Low Hole Effective Mass p-type Transparent Conducting Oxides, Supplementary information

Supplementary Figures

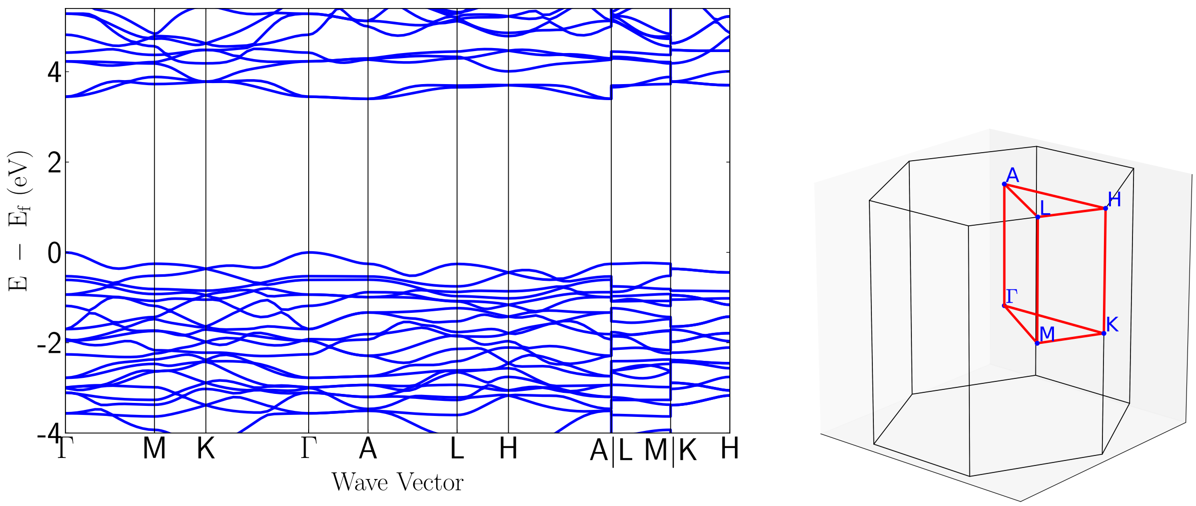

Supplementary Figure S1: **Band structure of $Tl_4V_2O_7$ (Materials project id: 3331).** The band structure is from DFT-GGA with a scissor operator (shift of the conduction band) applied to impose the GW band gap. The path in the Brillouin zone is also shown.

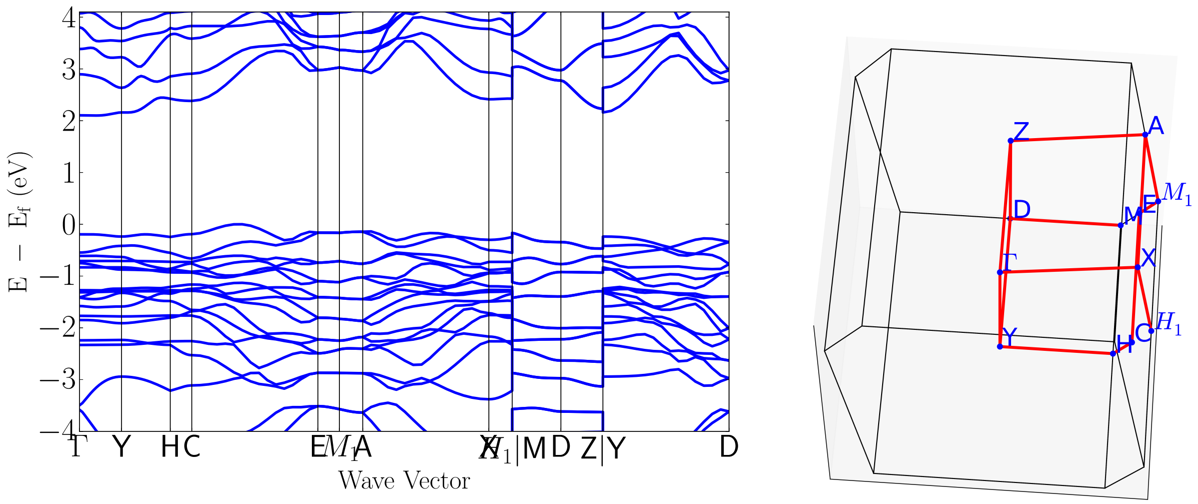

Supplementary Figure S2: **Band structure of Tl$_4$O$_3$ (Materials project id: 27684).** The band structure is from DFT-GGA with a scissor operator (shift of the conduction band) applied to impose the GW band gap. The path in the Brillouin zone is also shown.

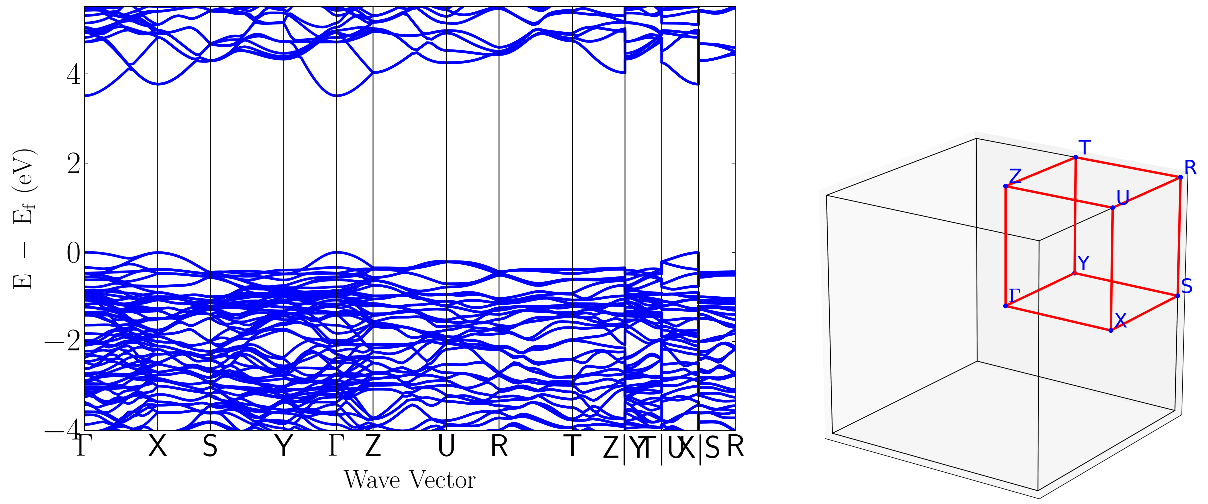

Supplementary Figure S3: **Band structure of $PbHfO_3$ (Materials project id: 22734).** The band structure is from DFT-GGA with a scissor operator (shift of the conduction band) applied to impose the GW band gap. The path in the Brillouin zone is also shown.

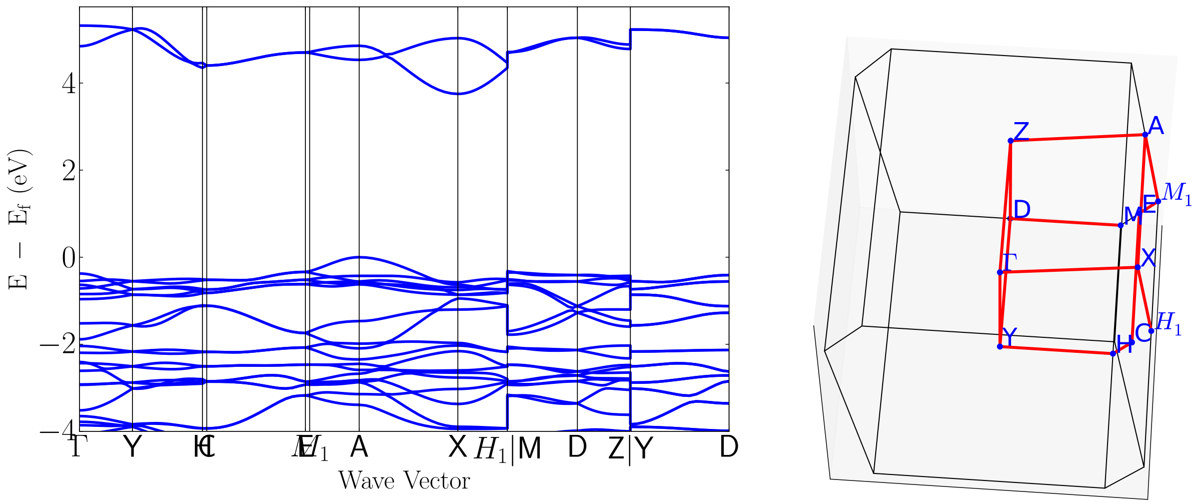

Supplementary Figure S4: **Band structure of Hg_2SO_4 (Materials project id: 7461).** The band structure is from DFT-GGA with a scissor operator (shift of the conduction band) applied to impose the GW band gap. The path in the Brillouin zone is also shown.

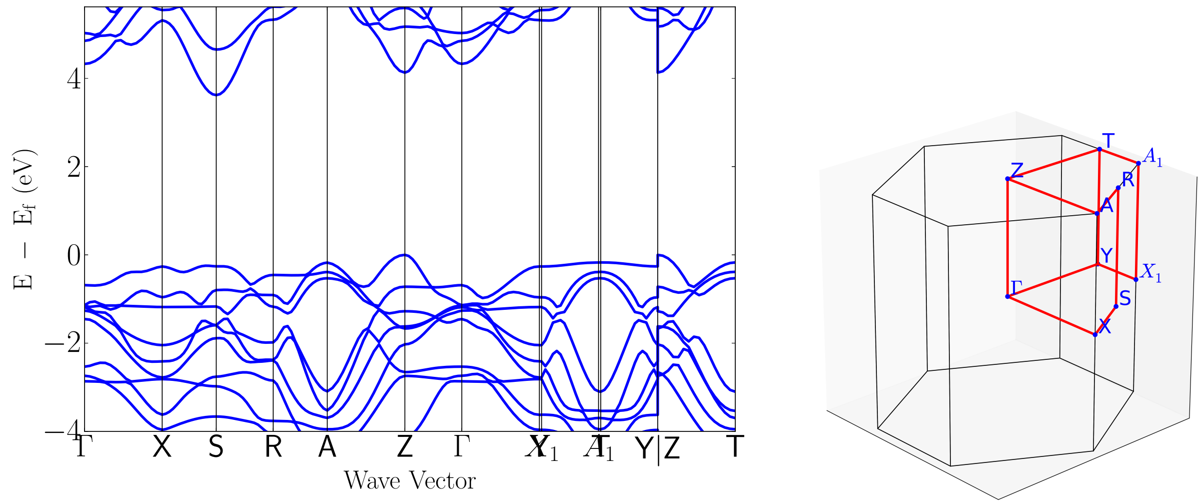

Supplementary Figure S5: **Band structure of PbZrO$_3$ (Materials project id: 20337).** The band structure is from DFT-GGA with a scissor operator (shift of the conduction band) applied to impose the GW band gap. The path in the Brillouin zone is also shown.

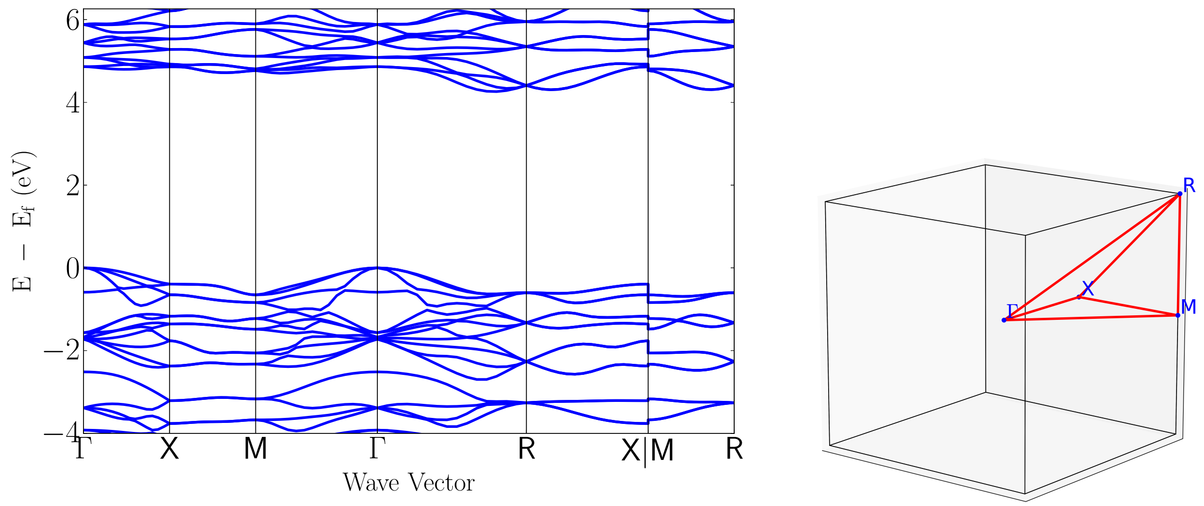

Supplementary Figure S6: **Band structure of ZrSO (Materials project id: 3519).** The band structure is from DFT-GGA with a scissor operator (shift of the conduction band) applied to impose the GW band gap. The path in the Brillouin zone is also shown.

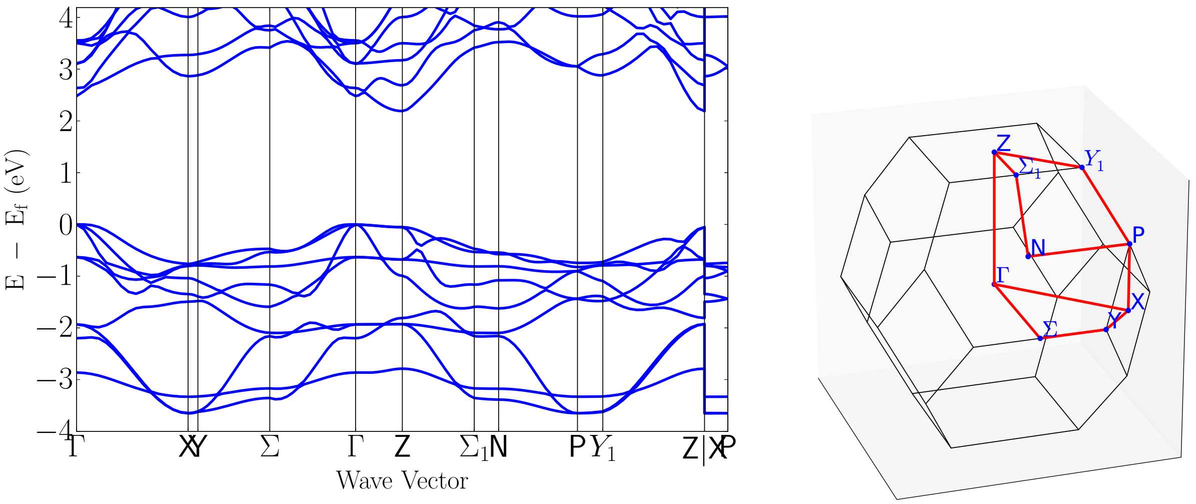

Supplementary Figure S7: **Band structure of Sr_4As_2O (Materials project id: 8299).** The band structure is from DFT-GGA with a scissor operator (shift of the conduction band) applied to impose the GW band gap. The path in the Brillouin zone is also shown.

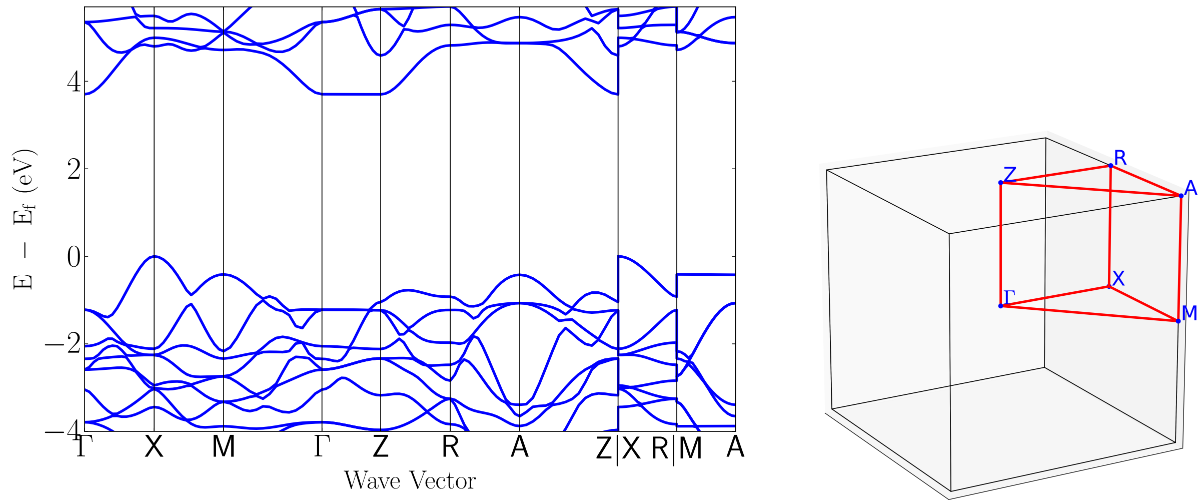

Supplementary Figure S8: **Band structure of $PbTiO_3$ (Materials project id: 20459).** The band structure is from DFT-GGA with a scissor operator (shift of the conduction band) applied to impose the GW band gap. The path in the Brillouin zone is also shown.

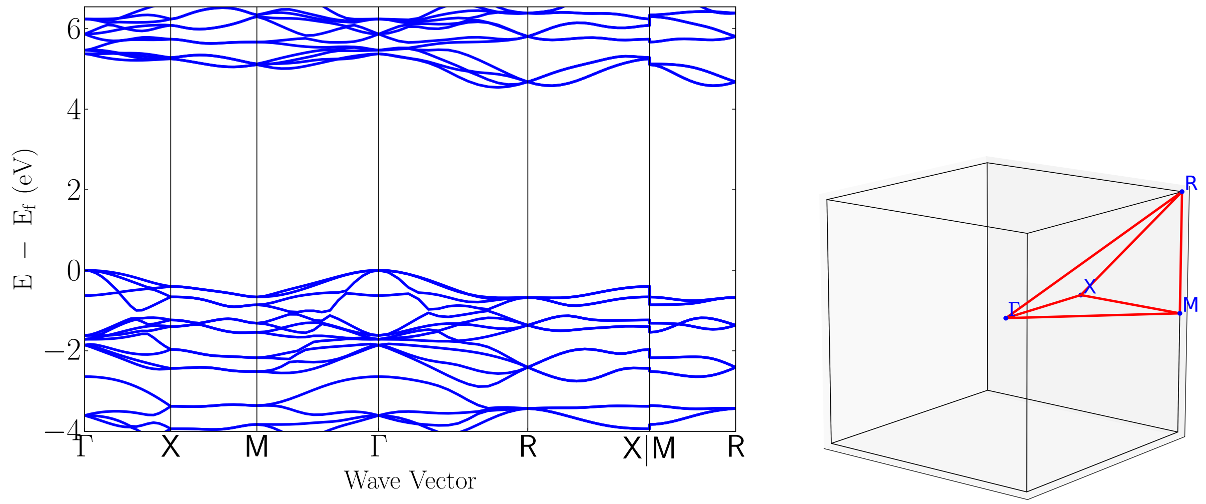

Supplementary Figure S9: **Band structure of HfSO (Materials project id: 7787).** The band structure is from DFT-GGA with a scissor operator (shift of the conduction band) applied to impose the GW band gap. The path in the Brillouin zone is also shown.

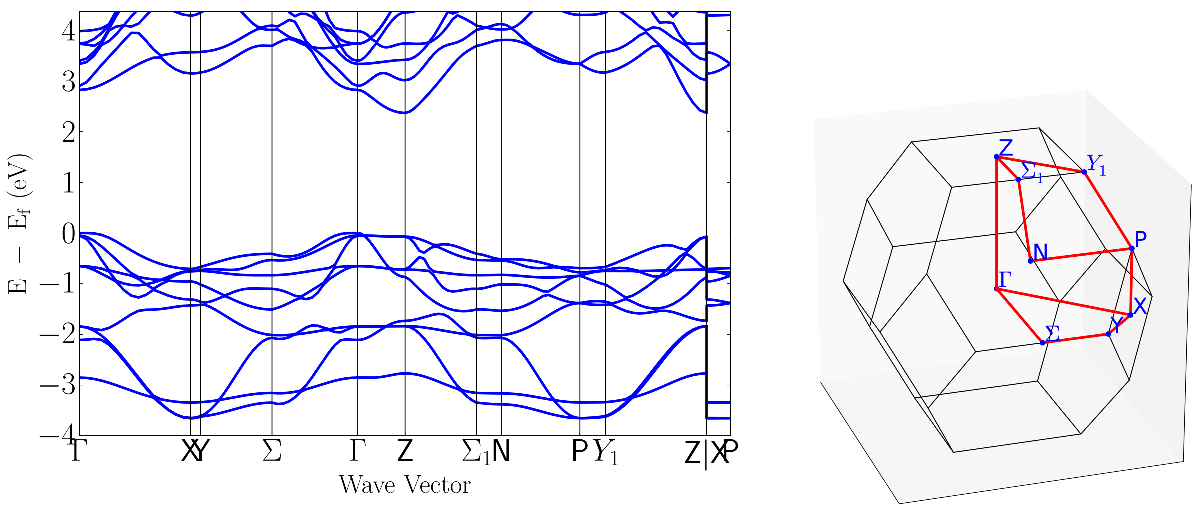

Supplementary Figure S10: **Band structure of Sr_4P_2O (Materials project id: 8298).** The band structure is from DFT-GGA with a scissor operator (shift of the conduction band) applied to impose the GW band gap. The path in the Brillouin zone is also shown.

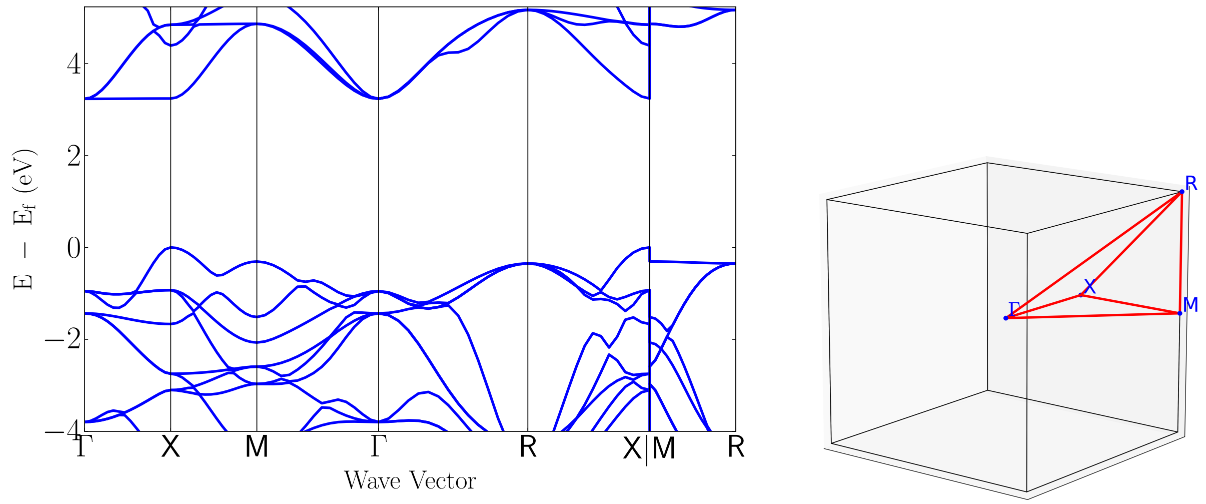

Supplementary Figure S11: **Band structure of $PbTiO_3$ (Materials project id: 21905).** The band structure is from DFT-GGA with a scissor operator (shift of the conduction band) applied to impose the GW band gap. The path in the Brillouin zone is also shown.

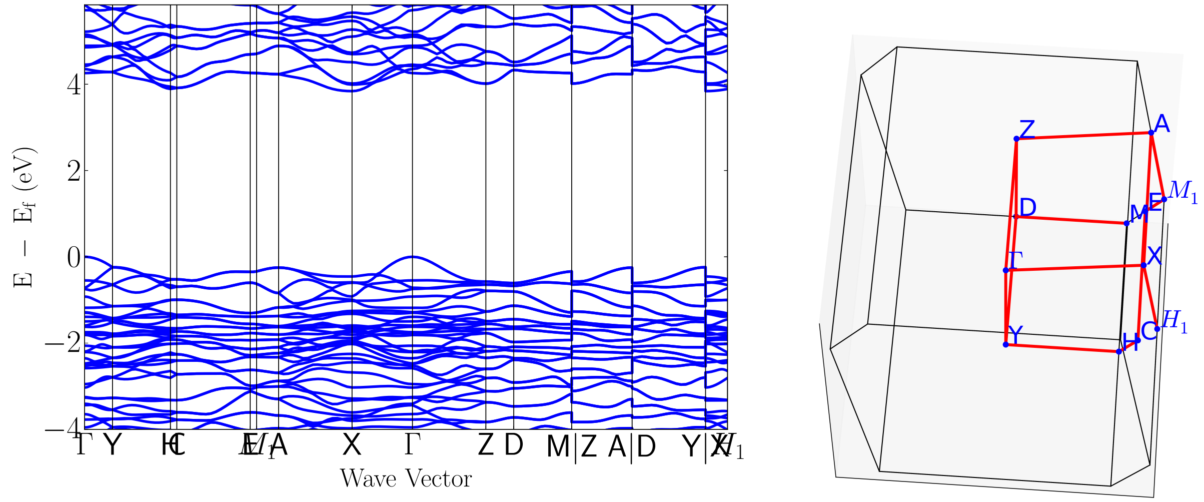

Supplementary Figure S12: **Band structure of $Sb_4Cl_2O_5$ (Materials project id: 23419).** The band structure is from DFT-GGA with a scissor operator (shift of the conduction band) applied to impose the GW band gap. The path in the Brillouin zone is also shown.

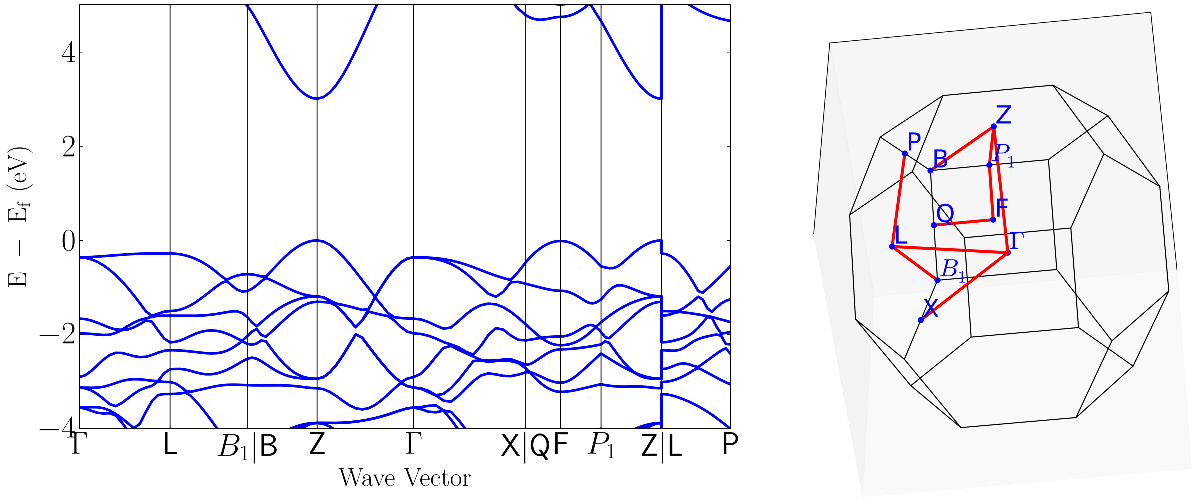

Supplementary Figure S13: **Band structure of B_6O (Materials project id: 1346).** The band structure is from DFT-GGA with a scissor operator (shift of the conduction band) applied to impose the GW band gap. The path in the Brillouin zone is also shown.

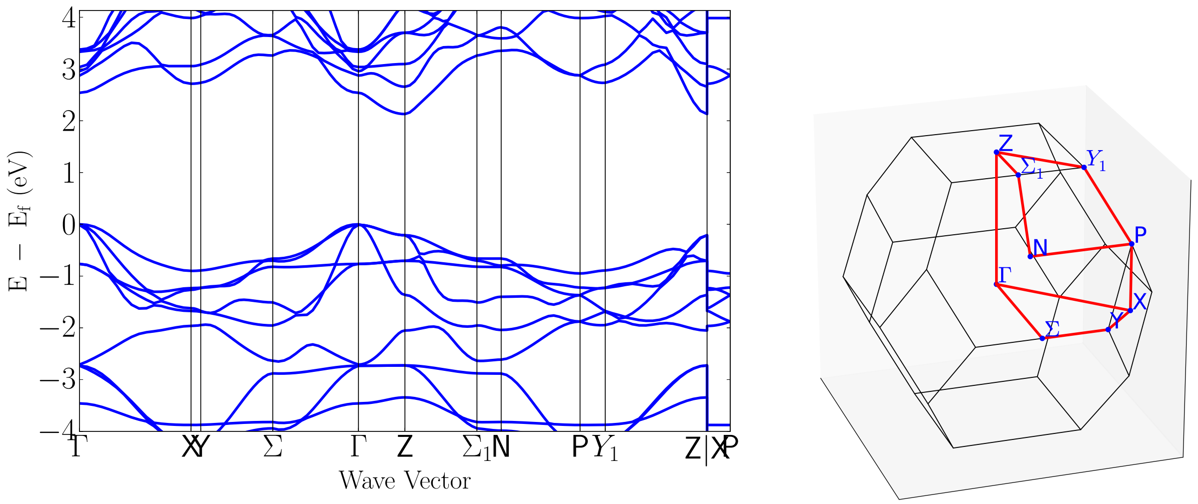

Supplementary Figure S14: **Band structure of Ca$_4$As$_2$O (Materials project id: 8789).** The band structure is from DFT-GGA with a scissor operator (shift of the conduction band) applied to impose the GW band gap. The path in the Brillouin zone is also shown.

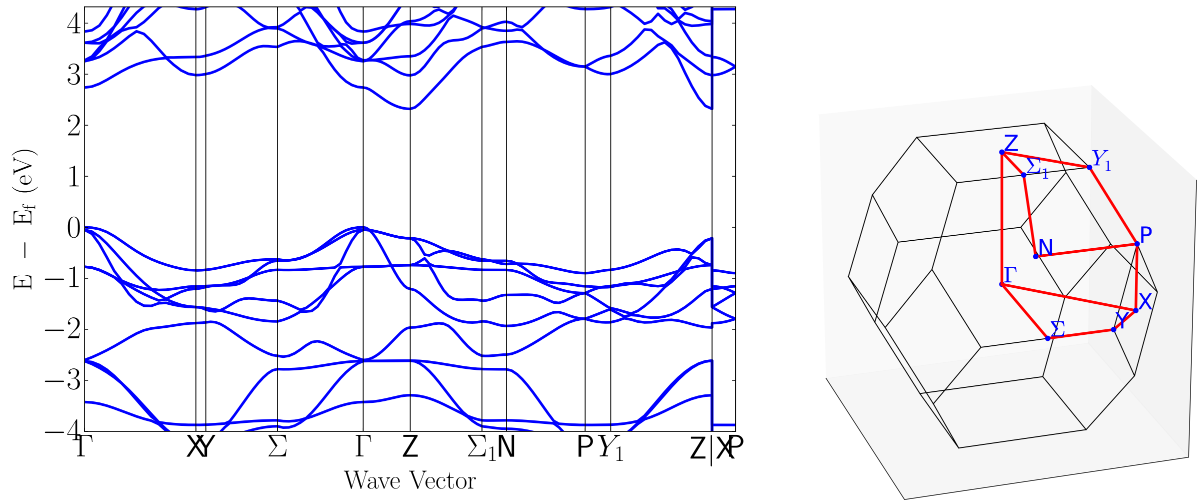

Supplementary Figure S15: **Band structure of Ca_4P_2O (Materials project id: 8789).** The band structure is from DFT-GGA with a scissor operator (shift of the conduction band) applied to impose the GW band gap. The path in the Brillouin zone is also shown.

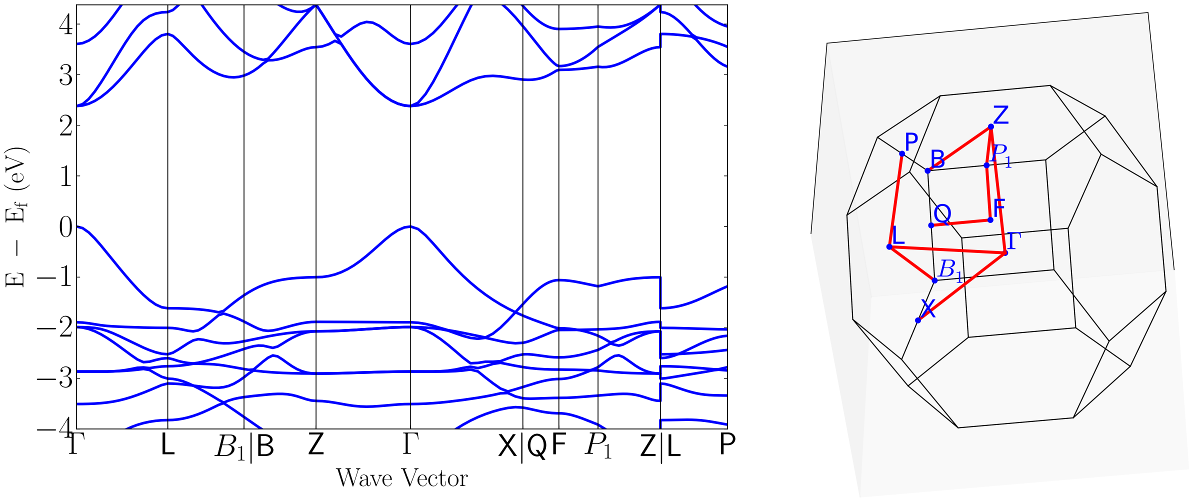

Supplementary Figure S16: **Band structure of $K_2Sn_2O_3$ (Materials project id: 7502).** The band structure is from DFT-GGA with a scissor operator (shift of the conduction band) applied to impose the GW band gap. The path in the Brillouin zone is also shown.

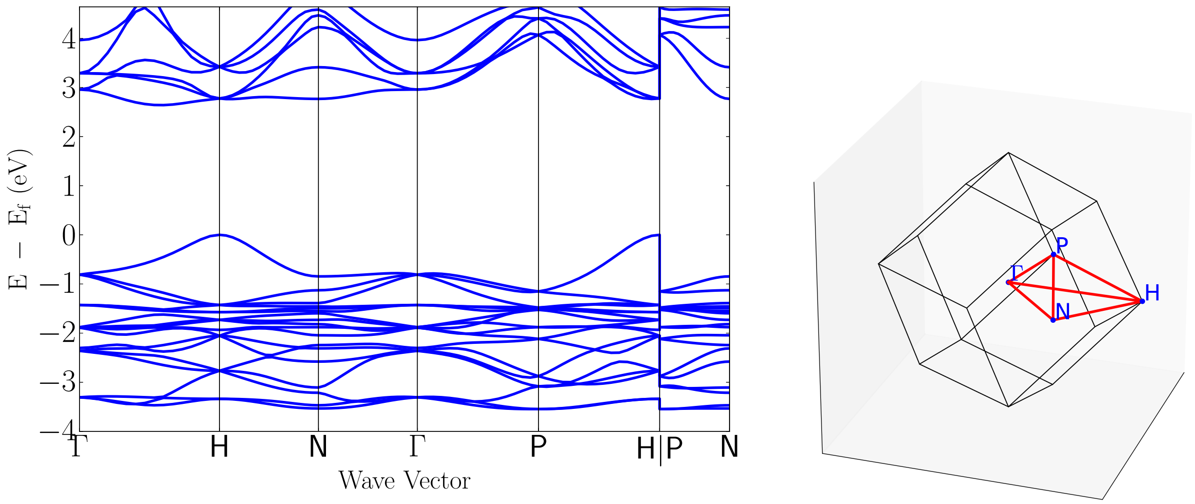

Supplementary Figure S17: **Band structure of $K_2Pb_2O_3$ (Materials project id: 20694).** The band structure is from DFT-GGA with a scissor operator (shift of the conduction band) applied to impose the GW band gap. The path in the Brillouin zone is also shown.

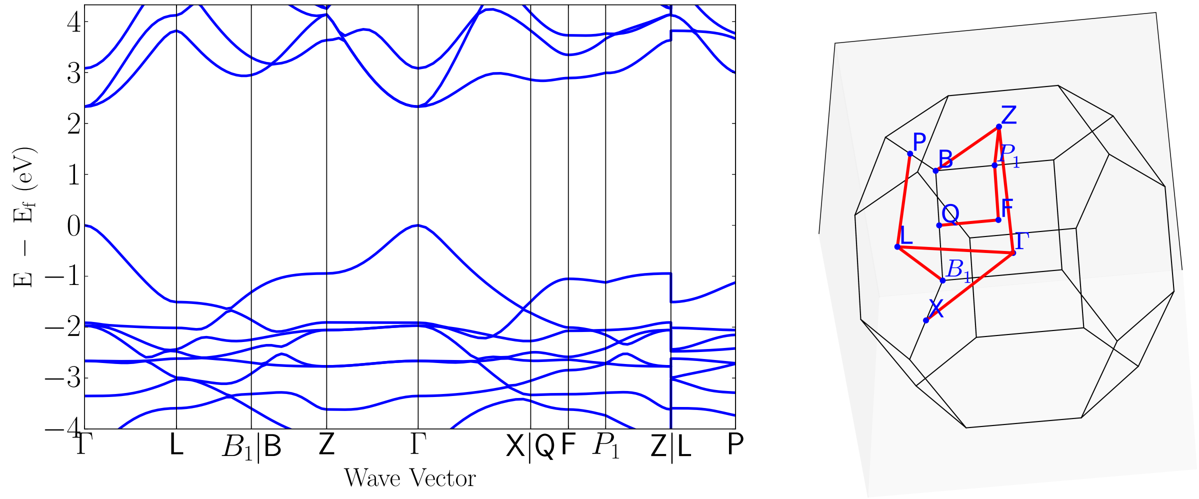

Supplementary Figure S18: **Band structure of $Rb_2Sn_2O_3$ (Materials project id: 7863).** The band structure is from DFT-GGA with a scissor operator (shift of the conduction band) applied to impose the GW band gap. The path in the Brillouin zone is also shown.

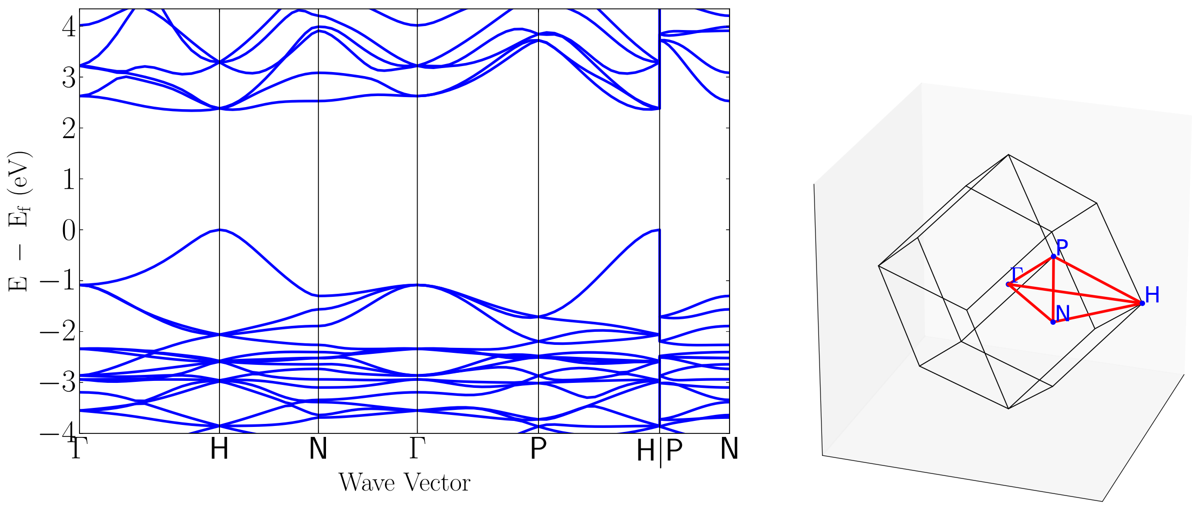

Supplementary Figure S19: **Band structure of $K_2Sn_2O_3$ (Materials project id: 8624).** The band structure is from DFT-GGA with a scissor operator (shift of the conduction band) applied to impose the GW band gap. The path in the Brillouin zone is also shown.

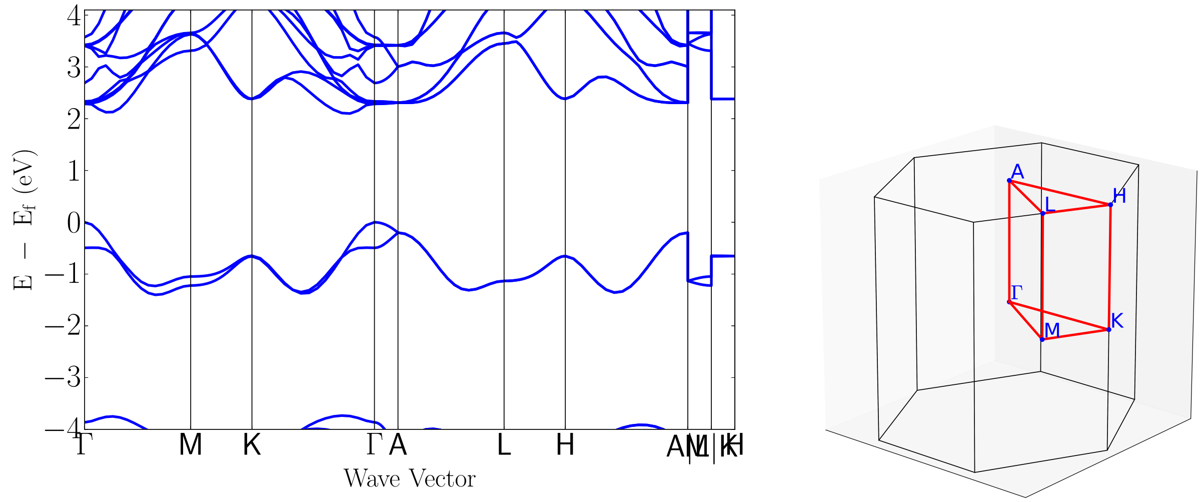

Supplementary Figure S20: **Band structure of $NaNbO_2$ (Materials project id: 3744).** The band structure is from DFT-GGA with a scissor operator (shift of the conduction band) applied to impose the GW band gap. The path in the Brillouin zone is also shown.

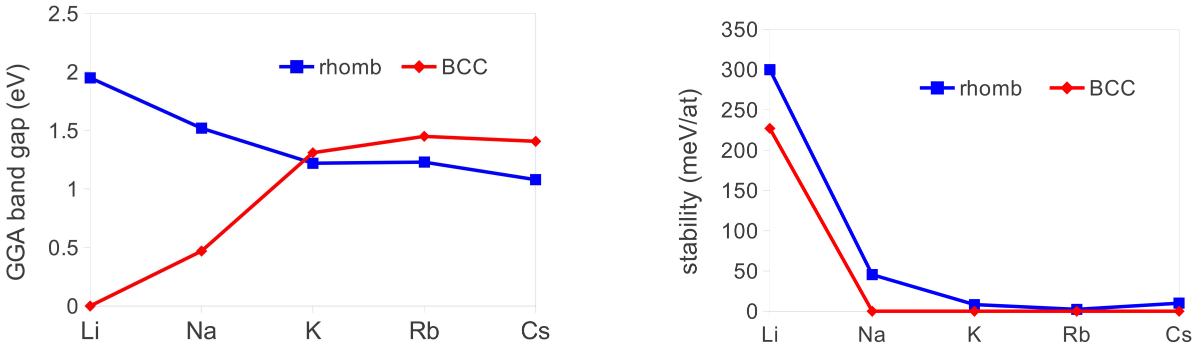

Supplementary Figure S21: **Band gap and stability of $A_2Sn_2O_3$ A=Li, Na, K, Rb, Cs rhombohedral and bcc structures.** The GGA Band gap (left) and stability in function of the alkali (right) for the bcc and rhombohedral phase of $K_2Sn_2O_3$. The stability represents the energy of the reaction for the decomposition to more stable products. Lower values indicate more stable compounds and a value of 0 meV/atom indicates a compound stable at 0K

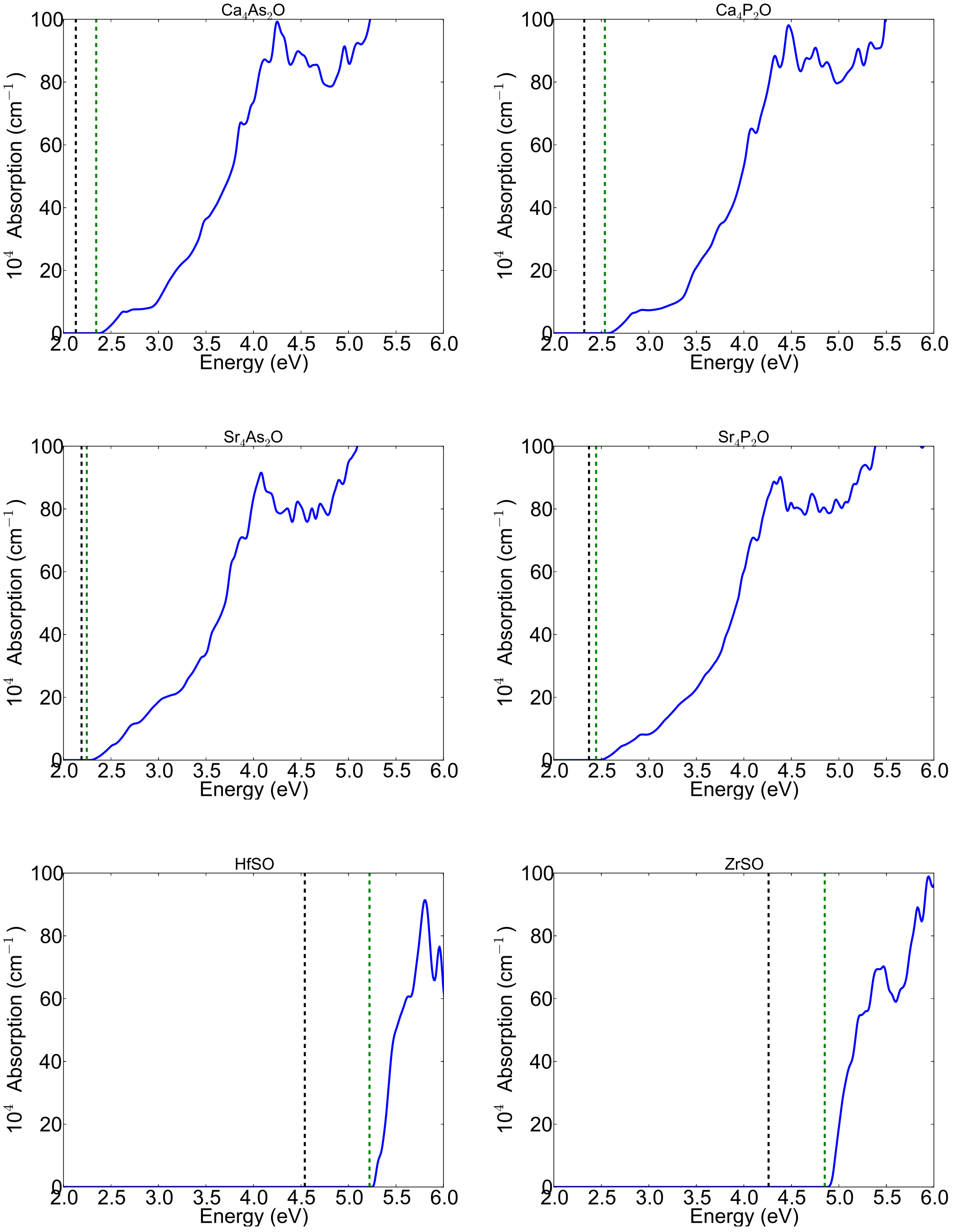
Ca_4As_2O
Ca_4P_2O
Sr_4As_2O
Sr_4P_2O
HfSO
ZrSO
10^4 Absorption (cm^{-1})
Energy (eV)
0
20
40
60
80
100
2.0
2.5
3.0
3.5
4.0
4.5
5.0
5.5
6.0

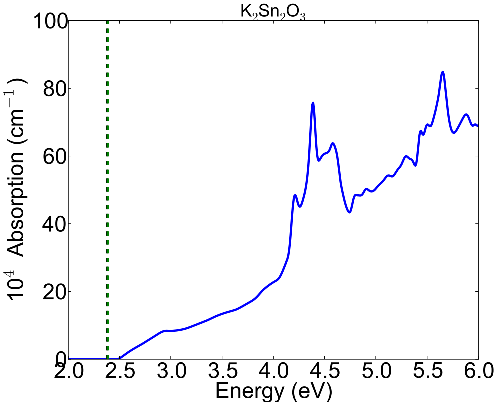
$K_2Sn_2O_3$

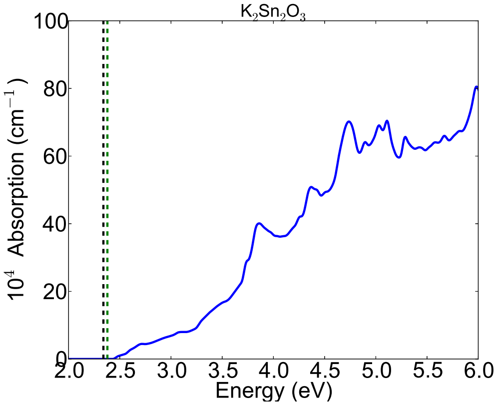
$K_2Sn_2O_3$

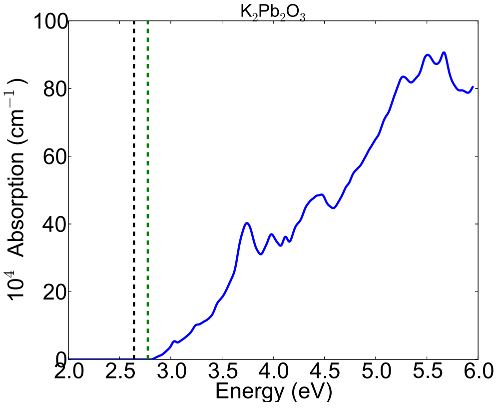
$K_2Pb_2O_3$

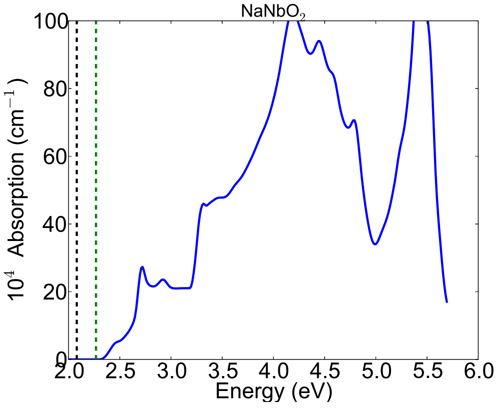
$NaNbO_2$

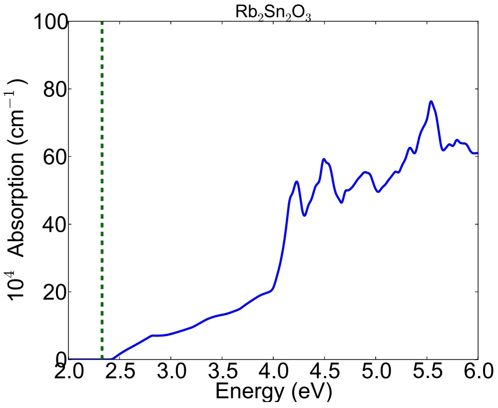
$Rb_2Sn_2O_3$

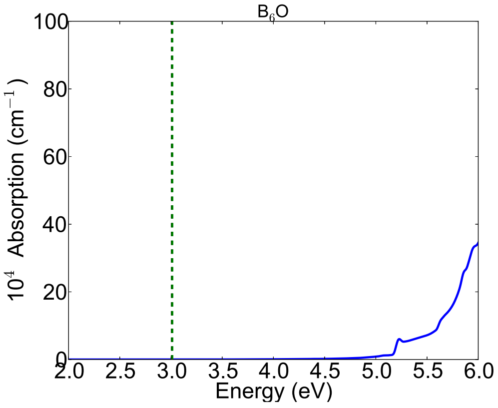
B_6O

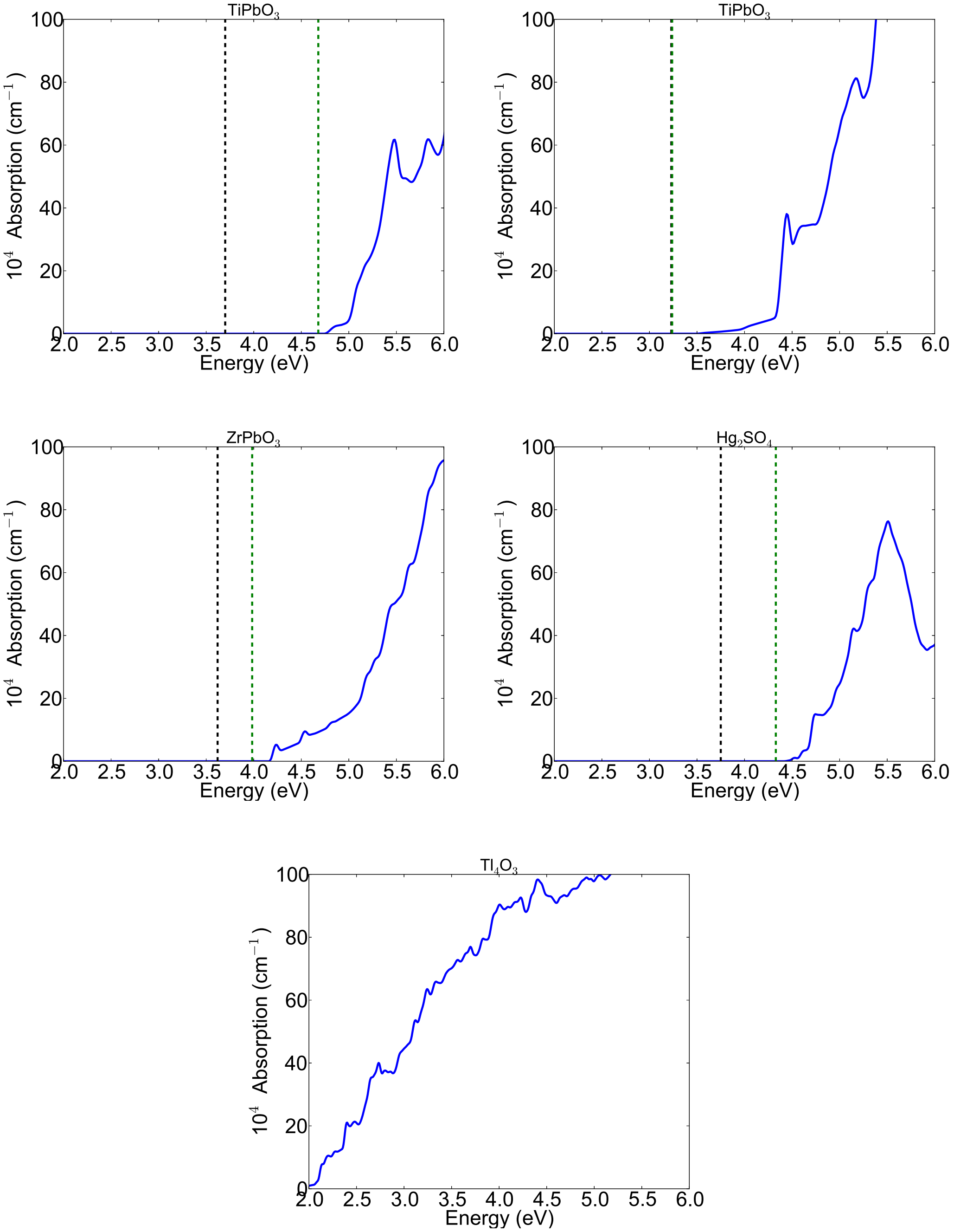

Supplementary Figure S22: **Absorption coefficient for each low hole effective mass candidates.** All the absorption coefficients have been computed within the RPA approximation on GGA results with VASP.[57] A scissor shift to make the band gap agree with GW results has been applied on all results. We follow a methodology close to the one from Yu *et al.*[56] No phonon-assisted transition or excitonic effects have been taken into account. The dark dashed line indicates the electronic band gap (direct or indirect) and the green dashed line the smallest direct electronic band gap.

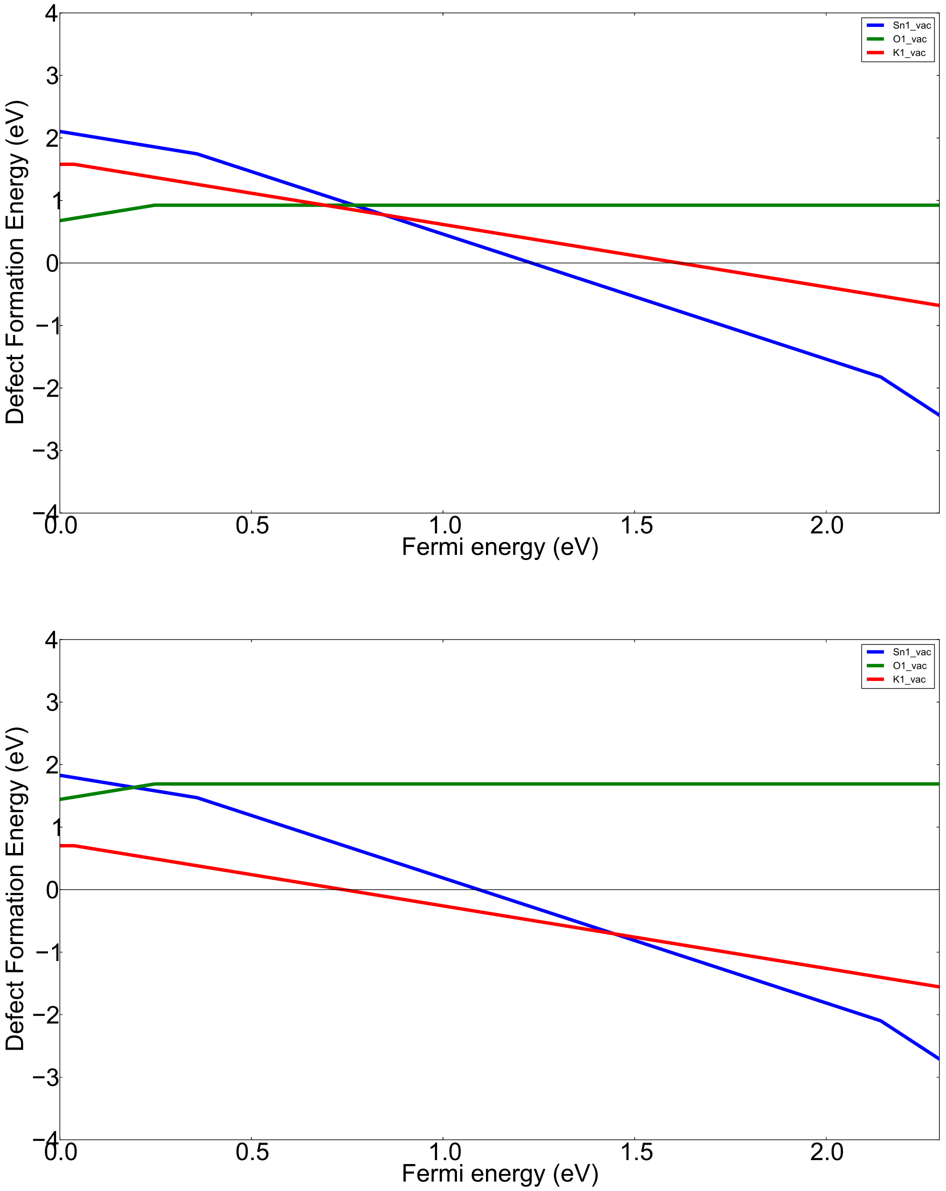

Supplementary Figure S23: **Formation energy vs fermi energy for $K_2Sn_2O_3$ bcc.** Both reducing (up) and oxidizing conditions (down) are shown.

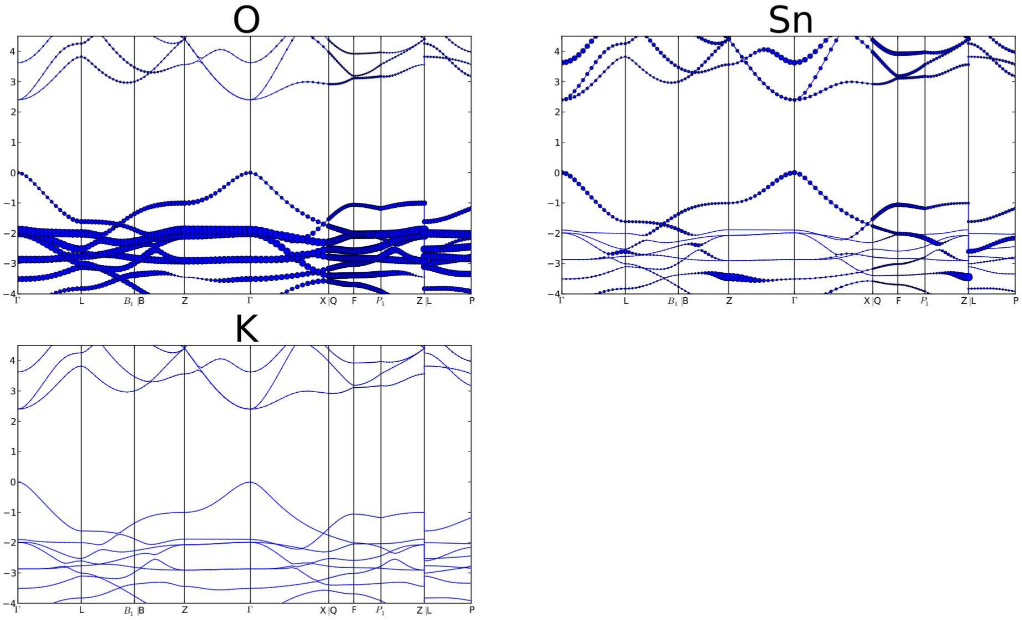

Supplementary Figure S24: **Projected band structures for $K_2Sn_2O_3$ rhombohedral.** The band structure is computed by GGA but a rigid shift of the conduction band (scissor operator) is applied to fit the band gap to the more accurate value obtained by GW. Each subfigure corresponds to the projection of the band structure on one element and the size of the dot indicates how strong is the element character. These plots are equivalent to the commonly called fat-band plots and provide the same information (without color scheme) than the Figure 4 of the main text.

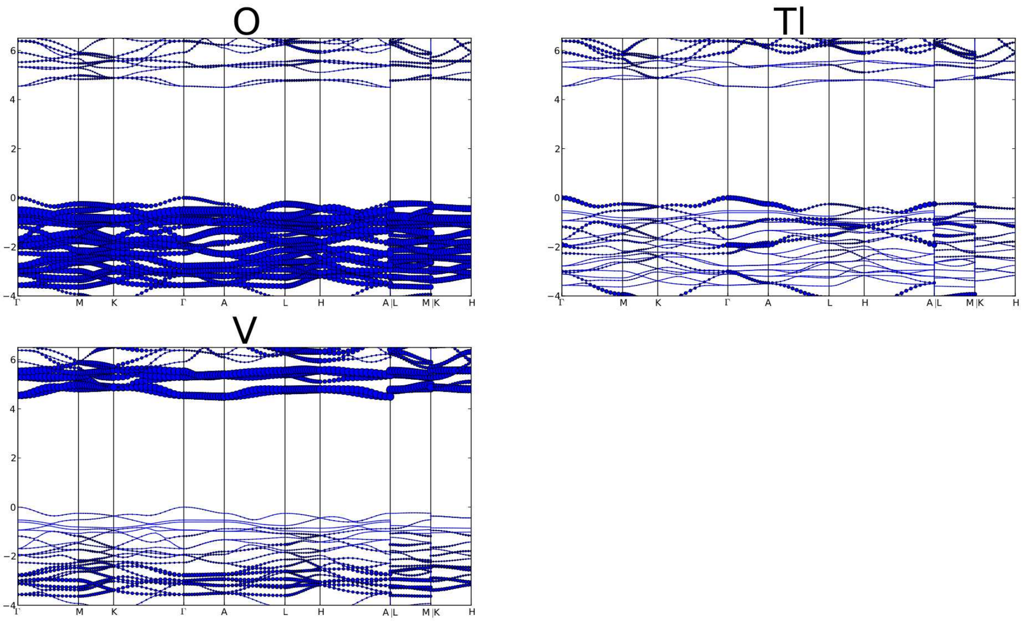

Supplementary Figure S25: **Projected band structures for $\mathbf{Tl_4V_2O_7}$.** The band structure is computed by GGA but a rigid shift of the conduction band (scissor operator) is applied to fit the band gap to the more accurate value obtained by GW. Each subfigure corresponds to the projection of the band structure on one element and the size of the dot indicates how strong is the element character. These plots are equivalent to the commonly called fat-band plots and provide the same information (without color scheme) than the Figure 4 of the main text.

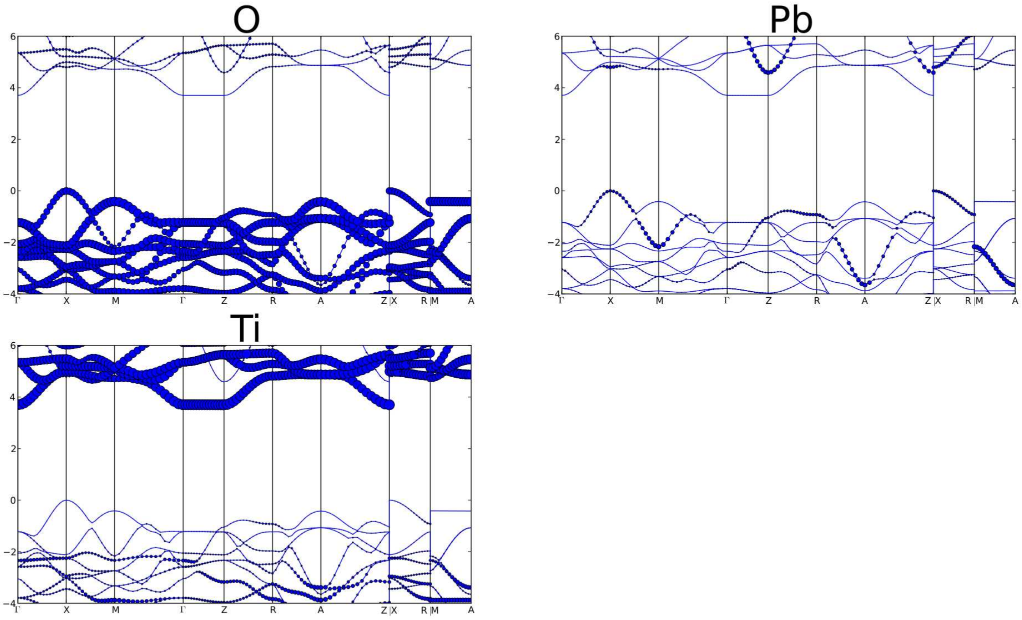

Supplementary Figure S26: **Projected band structures for $PbTiO_3$ tetragonal.** The band structure is computed by GGA but a rigid shift of the conduction band (scissor operator) is applied to fit the band gap to the more accurate value obtained by GW. Each subfigure corresponds to the projection of the band structure on one element and the size of the dot indicates how strong is the element character. These plots are equivalent to the commonly called fat-band plots and provide the same information (without color scheme) than the Figure 4 of the main text.

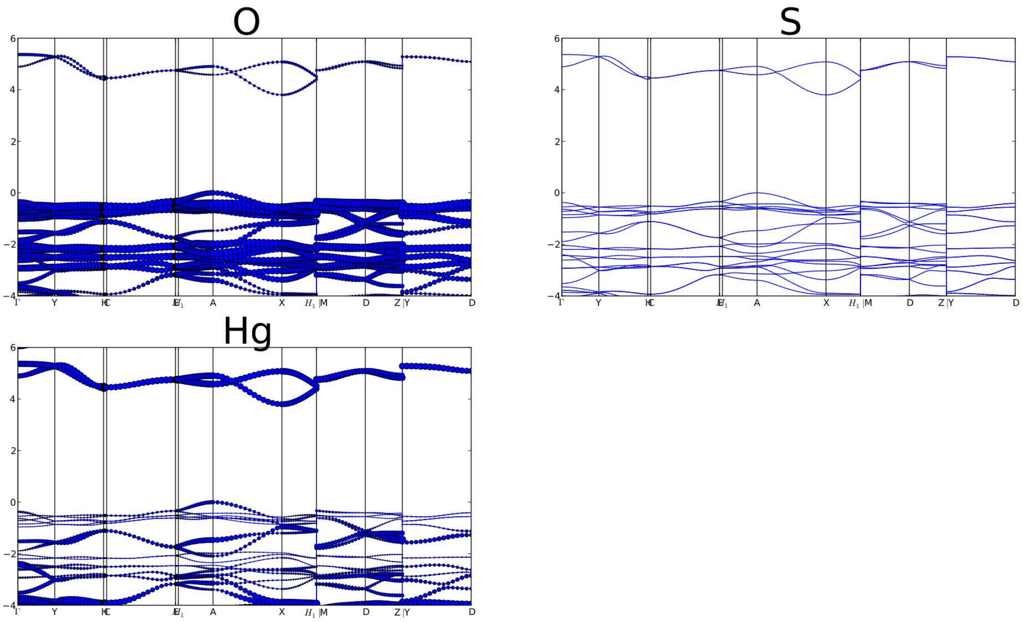

Supplementary Figure S27: **Projected band structures for $\mathbf{Hg_2SO_4}$.** The band structure is computed by GGA but a rigid shift of the conduction band (scissor operator) is applied to fit the band gap to the more accurate value obtained by GW. Each subfigure corresponds to the projection of the band structure on one element and the size of the dot indicates how strong is the element character. These plots are equivalent to the commonly called fat-band plots and provide the same information (without color scheme) than the Figure 4 of the main text.

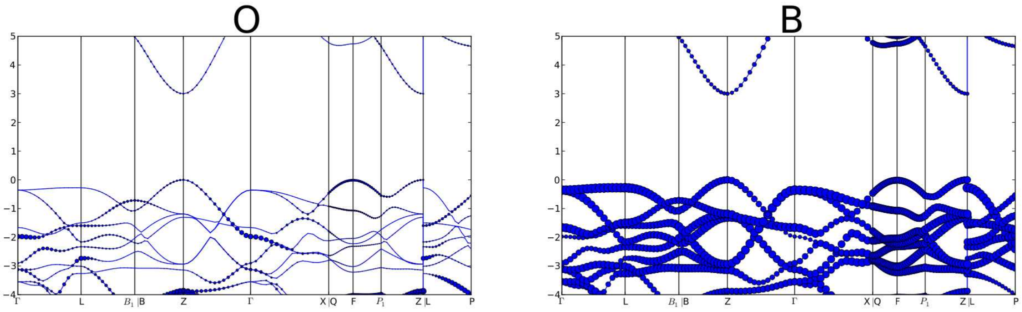

Supplementary Figure S28: **Projected band structures for B_6O.** The band structure is computed by GGA but a rigid shift of the conduction band (scissor operator) is applied to fit the band gap to the more accurate value obtained by GW. Each subfigure corresponds to the projection of the band structure on one element and the size of the dot indicates how strong is the element character. These plots are equivalent to the commonly called fat-band plots and provide the same information (without color scheme) than the Figure 4 of the main text.

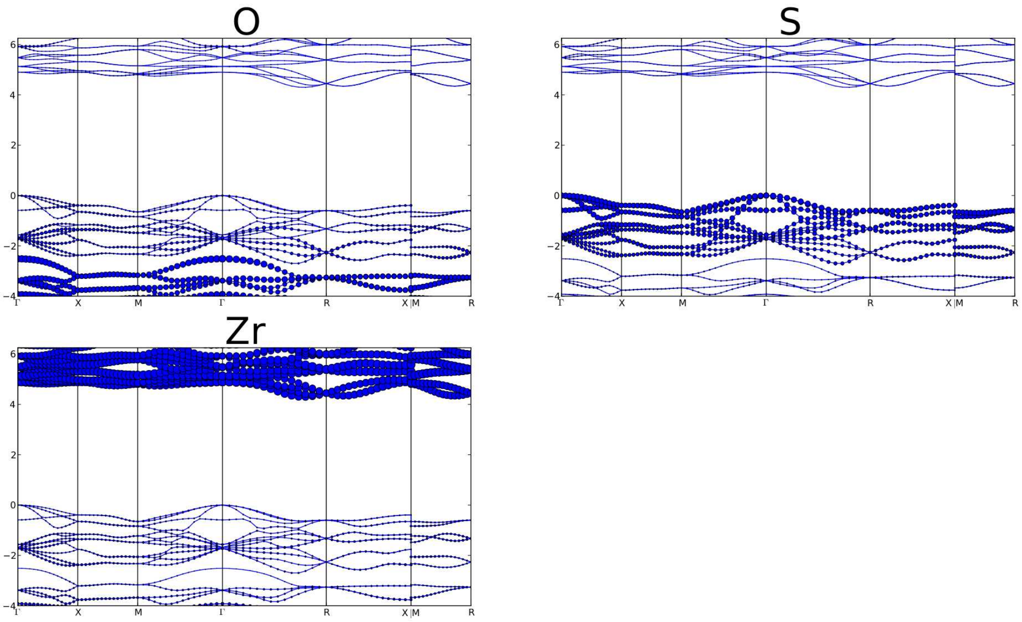

Supplementary Figure S29: **Projected band structures for ZrOS.** The band structure is computed by GGA but a rigid shift of the conduction band (scissor operator) is applied to fit the band gap to the more accurate value obtained by GW. Each subfigure corresponds to the projection of the band structure on one element and the size of the dot indicates how strong is the element character. These plots are equivalent to the commonly called fat-band plots and provide the same information (without color scheme) than the Figure 4 of the main text.

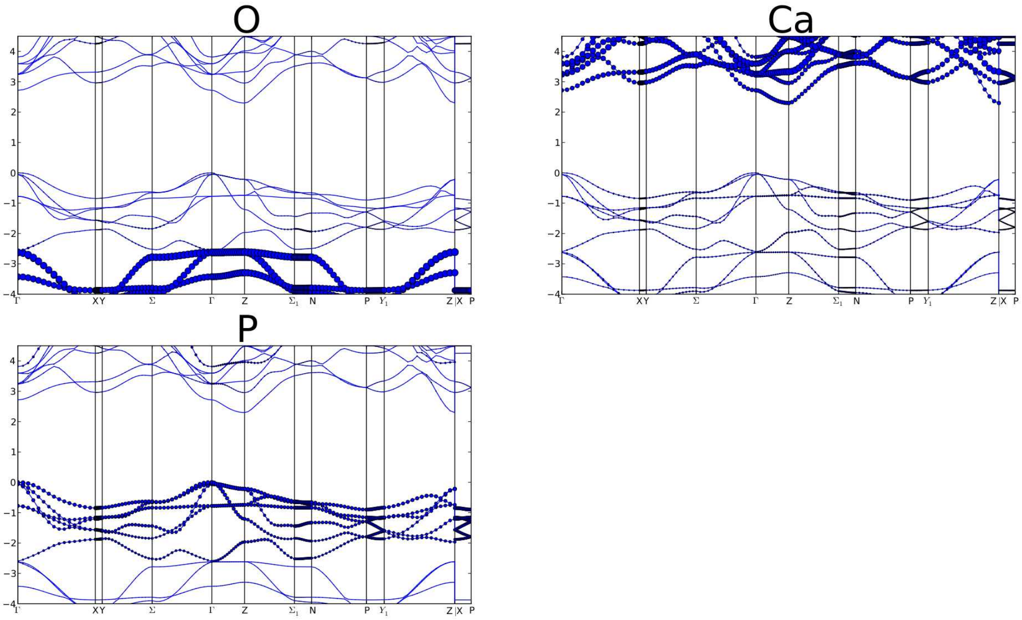

Supplementary Figure S30: **Projected band structures for Ca_4P_2O.** The band structure is computed by GGA but a rigid shift of the conduction band (scissor operator) is applied to fit the band gap to the more accurate value obtained by GW. Each subfigure corresponds to the projection of the band structure on one element and the size of the dot indicates how strong is the element character. These plots are equivalent to the commonly called fat-band plots and provide the same information (without color scheme) than the Figure 4 of the main text.

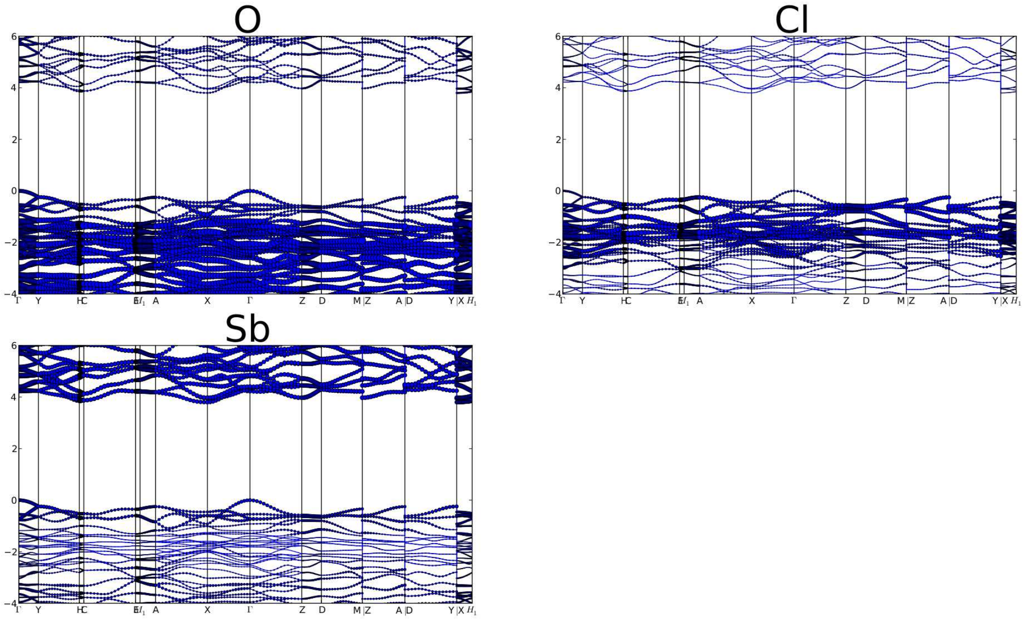

Supplementary Figure S31: **Projected band structures for $\mathbf{Sb_4Cl_2O_5}$.** The band structure is computed by GGA but a rigid shift of the conduction band (scissor operator) is applied to fit the band gap to the more accurate value obtained by GW. Each subfigure corresponds to the projection of the band structure on one element and the size of the dot indicates how strong is the element character. These plots are equivalent to the commonly called fat-band plots and provide the same information (without color scheme) than the Figure 4 of the main text.

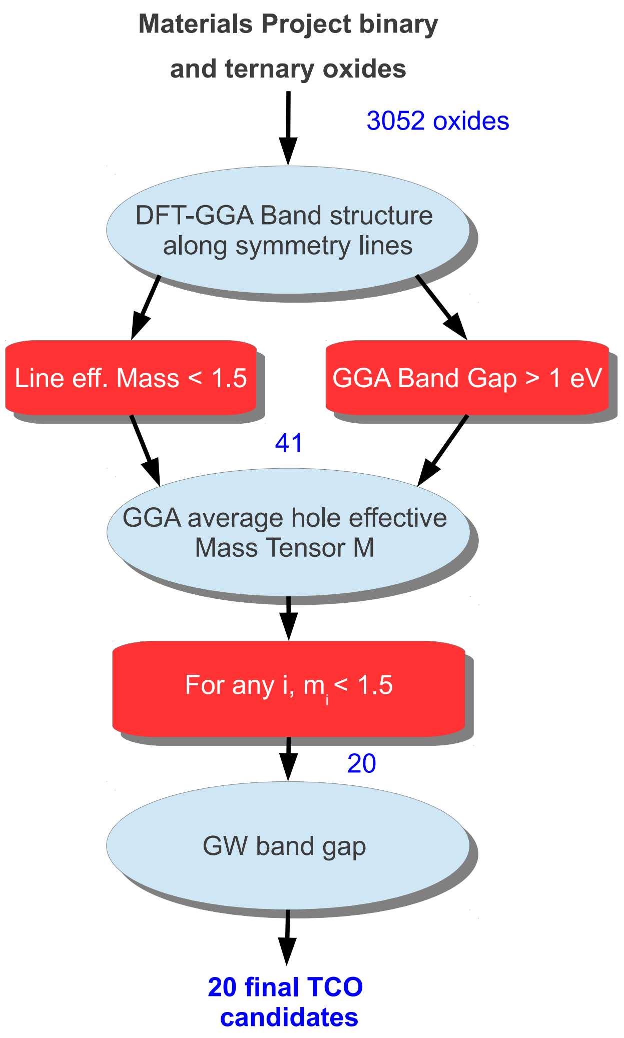

Supplementary Figure S32: **Flow chart of the tiered screening approach used for finding p-type TCOs.** Starting from a database of 3052 oxides, we performed DFT-GGA computations of band structures along symmetry lines. A first screening on line hole effective mass (< 1.5) and GGA band gap (> 1 eV) is performed, followed by computation of the full average effective mass tensor within GGA and GW band gap evaluation for the remaining compounds.

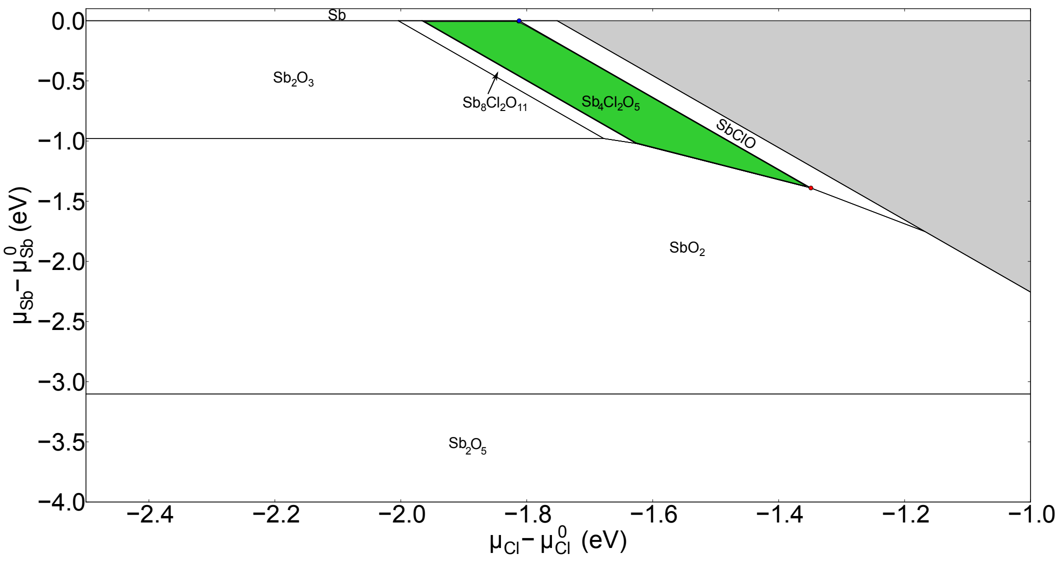

Supplementary Figure S33: **Chemical potential map for the Sb-Cl-O system.** The green region of Sb and Cl chemical potential indicates where the $Sb_4Cl_2O_5$ phase is stable. The blue and red points indicate respectively the most reducing and oxidizing conditions possible.

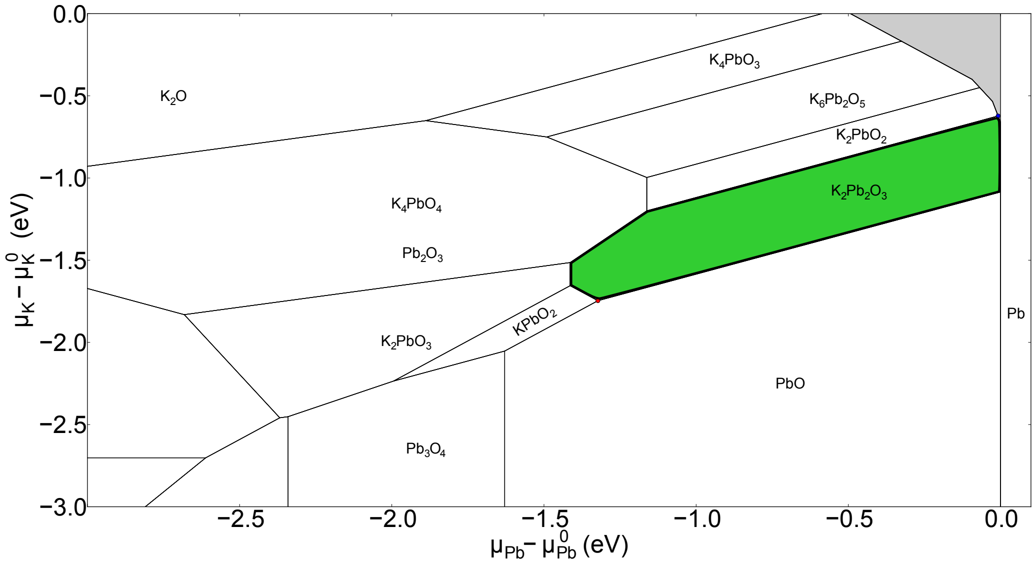

Supplementary Figure S34: **Chemical potential map for the K-Pb-O system.** The green region of K and Pb chemical potential indicates where the $K_2Pb_2O_3$ phase is stable. The blue and red points indicate respectively the most reducing and oxidizing conditions possible

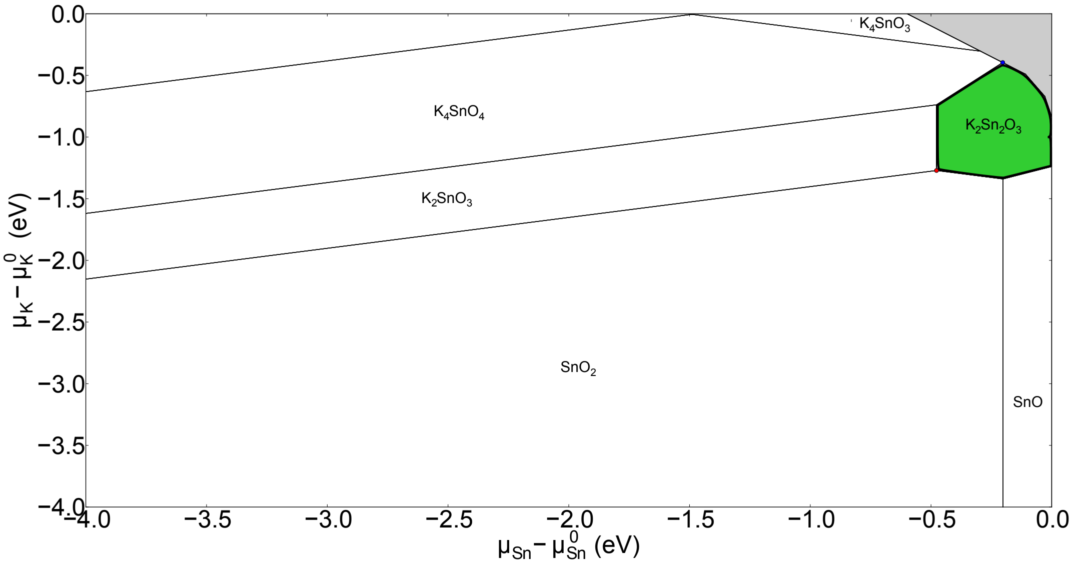

Supplementary Figure S35: **Chemical potential map for the K-Sn-O system.** The green region of K and Sn chemical potential indicates where the $K_2Sn_2O_3$ phase is stable. The blue and red points indicate respectively the most reducing and oxidizing conditions possible.

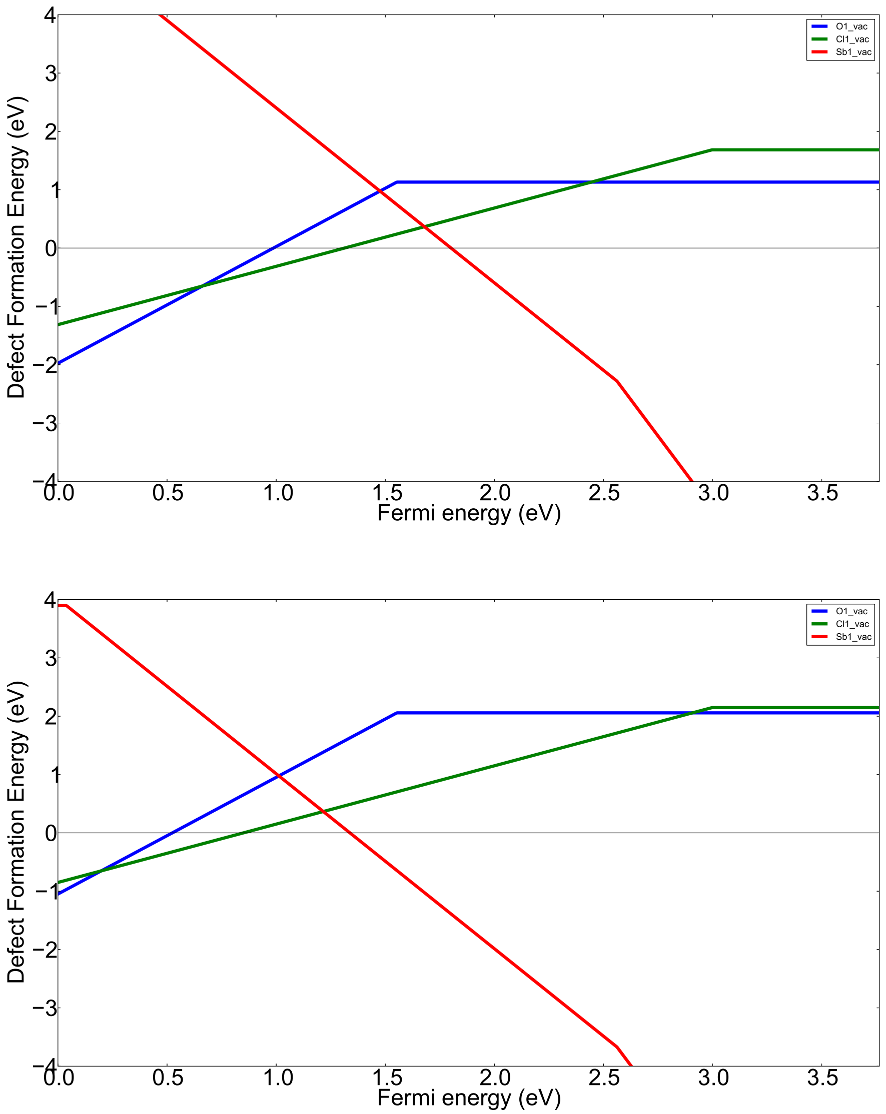

Supplementary Figure S36: **Formation energy vs fermi energy for $Sb_4Cl_2O_5$.** Both reducing (up) and oxidizing conditions (down) are shown.

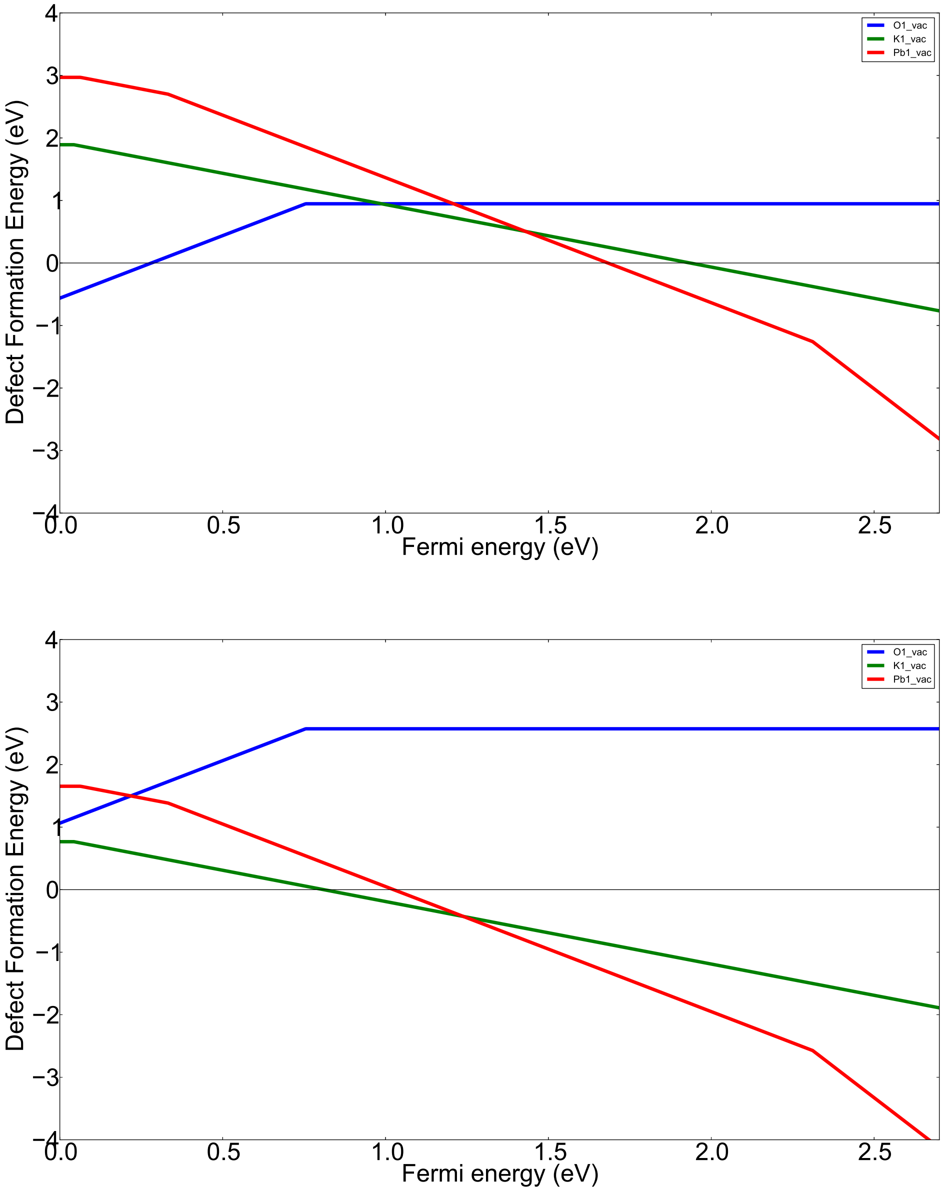

Supplementary Figure S37: **Formation energy vs fermi energy for $K_2Pb_2O_3$.** Both reducing (up) and oxidizing conditions (down) are shown.

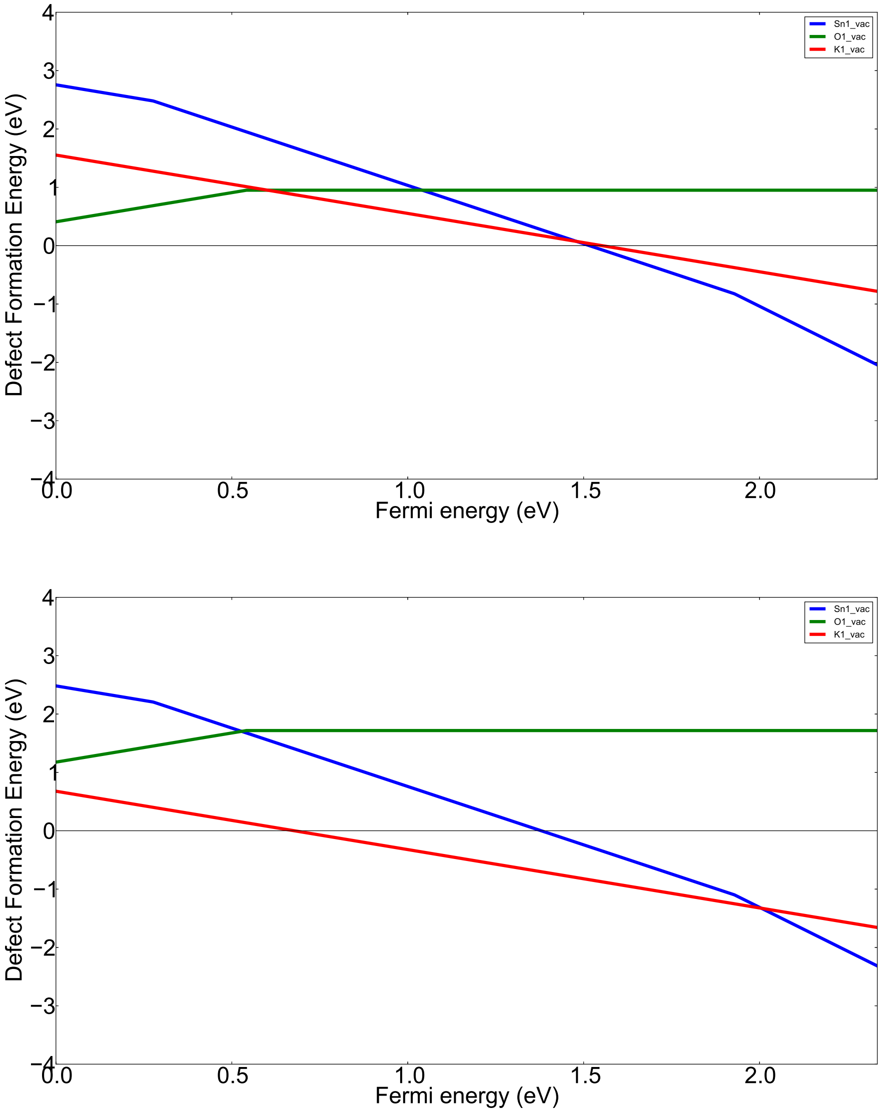

Supplementary Figure S38: **Formation energy vs fermi energy for $\mathbf{K_2Sn_2O_3}$ rhombohedral.** Both reducing (up) and oxidizing conditions (down) are shown.

Supplementary Tables

formula	ICSD number	Materials Project id	space group	band gap (eV)	line eff. mass	m_1	m_2	m_3
K2Sn2O3	40463	8624	I2_13(199)	1.31	0.29	0.27	0.27	0.27
Rb2Sn2O3	24816	7863	R-3m(166)	1.23	0.36	0.37	0.26	0.26
K2Pb2O3	1412	20694	I2_13(199)	1.69	0.41	0.39	0.39	0.39
K2Sn2O3	15511	7502	R-3m(166)	1.22	0.42	0.42	0.23	0.23
Ca4P2O1	402952	5380	I4/mmm(139)	1.27	0.57	1.19	1.19	0.56
Ca4As2O1	68203	8789	I4/mmm(139)	1.21	0.61	0.76	0.74	0.74
V1Bi1O4	62706	23044	I4_1/a(88)	2.12	0.69	1.91	1.91	0.86
B6O1	656231	1346	R-3m(166)	1.85	0.75	0.71	0.71	0.42
Sb4Cl2O5	2233	23419	P2_1/c(14)	2.64	0.78	0.49	0.41	0.27
Mg1Si1O3	156592	3547	Pbnm(62)	5.42	0.79	2.79	1.04	0.68
Ti1Pb1O3	27949	21905	Pm-3m(221)	1.58	0.80	0.48	0.48	0.48
Nb1N1O1	1031	7596	P2_1/c(14)	1.55	0.84	8.43	1.13	0.79
Sr4P2O1	33903	8298	I4/mmm(139)	1.21	0.87	1.36	1.36	0.83
Hf1S1O1	23327	7787	P2_13(198)	2.87	0.90	1.30	1.25	1.25
Ti1Pb1O3	162048	20459	P4mm(99)	1.82	0.90	1.09	0.48	0.48
P2Pt1O7	200871	29282	P2_1/c(14)	1.50	0.95	3.71	2.97	1.43
Sr4As2O1	33904	8299	I4/mmm(139)	1.19	0.96	1.46	0.80	0.80
Bi1Br1O1	29144	23072	P4/nmm(129)	2.27	0.96	3.85	1.3	1.3
Zr1S1O1	31721	3519	P2_13(198)	2.42	0.96	1.25	1.21	1.21
Zr1Pb1O3	39607	20337	C2mm(38)	2.67	1.00	1.09	0.98	0.44
Ag2Pb1O2	65998	20210	C2/c(15)	1.38	1.04	5.60	2.09	0.50
Hg2S1O4	15005	7461	P2/c(13)	1.98	1.06	1.37	0.93	0.33
La1Br1O1	84336	23023	P4/nmm(129)	3.73	1.06	1.56	1.56	1.23
Tl3B1O3	10196	4584	P6_3/m(176)	1.30	1.07	2.21	1.32	1.32

formula	ICSD number	Materials Project id	space group	band gap (eV)	line eff. mass	m_1	m_2	m_3
Tl3V1O4	80667	29047	Im2m(44)	2.54	1.08	1.91	1.45	0.67
Hf1Pb1O3	161707	22734	Pcma(55)	2.72	1.08	1.08	0.83	0.73
Tl4O3	23478	27684	P2_1/m(11)	1.10	1.12	1.16	1.03	0.88
Ti4Bi2O11	79769	28962	C2/m(12)	2.04	1.16	54.80	1.65	0.96
Tl4V2O7	72810	3331	P-3m1(164)	2.44	1.19	1.44	0.62	0.62
Sc2O3	160203	13060	P-3m1(164)	3.39	1.21	1.25	1.25	0.67
Pt1O2	76431	617	P-3m1(164)	1.60	1.24	10.83	2.29	2.29
Tl3P1O4	60780	5709	P6_3(173)	2.64	1.25	2.37	2.37	1.42
Ti1Sn2O4	163230	18288	P4_2/mbc(135)	1.08	1.27	1.54	1.54	0.61
Na1Nb1O2	300244	3744	P6_3/mmc(194)	1.38	1.32	1.36	0.64	0.64
Sb2S2O1	68346	28711	P-1(2)	1.24	1.38	8.41	3.52	1.18
K1I1O3	20198	23487	P1(1)	2.77	1.44	1.68	1.60	0.89
V2Pb3O8	67605	19903	C2(5)	2.79	1.44	2.69	2.04	1.13
Y2Sn2O7	160115	3370	Fd-3m(227)	2.75	1.45	2.08	2.08	2.08
La2Sn2O7	153813	4086	Fd-3m(227)	2.67	1.46	2.22	2.22	2.22
Li2Ti1O3	162215	2931	C2/c(15)	3.03	1.46	2.82	2.77	1.31
Y2Ti1O5	34692	17559	Pmnb(62)	3.27	1.29	16.9	1.32	1.11
La1O1F1	30622	8111	R-3m(166)	4.22	1.46	846.48	1.56	1.56

Supplementary Table S1: **Low line hole effective mass oxides.** Oxides with line hole effective mass (computed according to equation (S6)) lower than 1.5 (and a band gap larger than 1 eV) among the 3052 oxides in our data set. The compounds are sorted from lowest to highest hole effective mass. For each of those 42 compounds, a full average hole effective mass tensor has been computed using equation (S5) and the results are presented in the last column. We did not consider Sc_2O_3 in the $P\bar{3}m$ structure (ICSD 160230) further in this work as this ICSD entry turned out to come from an *ab initio* computation and was never observed experimentally. Moreover, it is computed to be very unstable (the energy above the convex hull at 0K is around 132 meV/atom) and unlikely to be synthesizable. Among the 41 candidates identified by line effective mass, we found 20 final candidates with none of their principal effective masses higher than 1.5.

formula	**ICSD number**	**space group**	**band gap (eV)**	**effective mass**				
				$\mathbf{m_1}$	$\mathbf{m_2}$	$\mathbf{m_3}$	$\mathbf{m_{min}}$	$\mathbf{m_{max}}$
$K_2Sn_2O_3$	40463	$\mathrm{I2_13}$(199)	2.3	0.27	0.27	0.27	0.27	0.27
$K_2Sn_2O_3$	15511	$\mathrm{R\bar{3}m}$ (166)	2.4	0.42	0.23	0.23	0.27	0.28
$Rb_2Sn_2O_3$	24816	$\mathrm{R\bar{3}m}$ (166)	2.3	0.37	0.26	0.26	0.29	0.29
$Sb_4Cl_2O_5$	2233	$\mathrm{P2_1/c}$(14)	3.8	0.49	0.41	0.27	0.37	0.38
$K_2Pb_2O_3$	1412	$\mathrm{I2_13}$(199)	2.6	0.39	0.39	0.39	0.39	0.39
$PbTiO_3$	27949	$\mathrm{Pm\bar{3}m}$ (221)	3.2	0.48	0.48	0.48	0.48	0.48
B_6O	656231	$\mathrm{R\bar{3}m}$ (166)	3.0	0.71	0.71	0.42	0.59	0.59
$PbTiO_3$	162048	P4mm(99)	3.7	1.09	0.48	0.48	0.6	0.62
Ca_4As_2O	68203	I4/mmm(139)	2.1	0.76	0.74	0.74	0.75	0.75
Hg_2SO_4	15005	P2/c(13)	3.8	1.37	0.93	0.33	0.68	0.75
$PbZrO_3$	39607	C2mm(38)	3.6	1.09	0.98	0.44	0.74	0.77
$NaNbO_2$	300244	$\mathrm{P6_3/mmc}$(194)	2.1	1.36	0.64	0.64	0.8	0.82
$Tl_4V_2O_7$	72810	$\mathrm{P\bar{3}m1}$(164)	4.5	1.44	0.62	0.62	0.8	0.82
$PbHfO_3$	161707	Pcma(55)	3.5	1.08	0.83	0.73	0.86	0.86
Ca_4P_2O	402952	I4/mmm(139)	2.3	1.19	1.19	0.56	0.9	0.92
Sr_4As_2O	33904	I4/mmm(139)	2.2	1.46	0.8	0.8	0.96	0.97
Tl_4O_3	23478	$\mathrm{P2_1/m}$(11)	1.6	1.16	1.03	0.88	1.02	1.02
Sr_4P_2O	33903	I4/mmm(139)	2.4	1.36	1.36	0.83	1.14	1.15
ZrSO	31721	$\mathrm{P2_13}$(198)	4.3	1.25	1.21	1.21	1.23	1.23
HfSO	23327	$\mathrm{P2_13}$(198)	4.5	1.3	1.25	1.25	1.27	1.27

Supplementary Table S2: Hole effective masses and computed GW band gaps for all low hole effective mass candidates. The m_1, m_2, m_3 values indicate the eigenvalues of the average effective mass tensor. m_{min} and m_{max} are upper and lower bound to the effective mass in a polycrystalline film (see Supplementary Methods).

formula	**ICSD number**	**space group**	**band gap (eV)**	**effective mass**				
				m_1	**m_2**	**m_3**	**m_{min}**	**m_{max}**
$AlCuO_2$	60844	$R\bar{3}m$ (166)	3, [60]	5.2	1.91	1.91	2.53	2.64
$SrCu_2O_2$	25002	$I4_1/amd$ (141)	3.3, [17]	5.27	1.39	1.39	2.01	2.22
$ZnRh_2O_4$	109298	$Fd\bar{3}m$ (227)	2.7, [61]	3.47	3.47	3.47	3.47	3.47
Cu_2O	172174	$P\bar{3}m$ (224)	2.1, [2]	1.55	1.55	1.55	1.55	1.55

Supplementary Table S3: **Hole effective masses and experimental band gaps for a few known p-type oxides of interest.** m_{min} and m_{max} are upper and lower bound to the effective mass in a polycrystalline film (see Supplementary Methods).

formula	**ICSD number**	**space group**	$\mathbf{m_1}$	$\mathbf{m_2}$	$\mathbf{m_3}$	**band gap (eV)**
In_2O_3	640179	Ia3(206)	0.17	0.17	0.17	2.9, [27]
ZnO	163380	$P6_3mc(186)$	0.16	0.16	0.16	3.4[62]
SnO_2	157449	$P4_2/mnm$	0.18	0.18	0.16	3.6[63]

Supplementary Table S4: **Electron effective mass and experimental band gaps for a few known *n*-type TCOs.** The m_1, m_2, m_3 values indicate the eigenvalues of the average effective mass tensor.

element	**Z**	**electronic configuration**	**pseudopotential valence configuration**	**pseudopotential scheme**
B	5	[He] $2s^2 2p^1$	$2s^2 2p^1$	TM
O	8	[He] $2s^2 2p^4$	$2s^2 2p^4$	TM
Na	11	[Ne] $3s^1$	$2s^2 2p^6 3s^1$	HGH
P	15	[Ne] $3s^2 3p^3$	$3s^2 3p^3$	TM
S	16	[Ne] $3s^2 3p^4$	$3s^2 3p^4$	HGH
Cl	17	[Ne] $3s^2 3p^5$	$3s^2 3p^5$	TM
K	19	[Ar] $4s^1$	$3s^2 3p^6 4s^1$	HGH
Ca	20	[Ar] $4s^2$	$3s^2 3p^6 4s^2$	HGH
Ti	22	[Ar] $3d^2 4s^2$	$3s^2 3p^6 3d^2 4s^2$	HGH
V	23	[Ar] $3d^3 4s^2$	$3s^2 3p^6 3d^3 4s^2$	HGH
As	33	[Ar] $3d^{10} 4s^2 4p^3$	$4s^2 4p^3$	TM
Rb	37	[Kr] $5s^1$	$4s^2 4p^6 5s^1$	HGH
Sr	38	[Kr] $5s^2$	$4s^2 4p^6 5s^2$	HGH
Zr	40	[Kr] $4d^2 5s^2$	$4s^2 4p^6 4d^2 5s^2$	HGH
Nb	41	[Kr] $4d^4 5s^1$	$4s^2 4p^6 4d^4 5s^2$	HGH
Sn	50	[Kr] $4d^{10} 5s^2 5p^2$	$4s^2 4p^6 4d^{10} 5s^2 5p^2$	TM
Sb	51	[Kr] $4d^{10} 5s^2 5p^3$	$5s^2 5p^3$	TM
Hf	72	[Xe] $4f^{14} 5d^2 6s^2$	$5s^2 5p^6 5d^2 6s^2$	HGH
Hg	80	[Xe] $4f^{14} 5d^{10} 6s^2$	$5d^{10} 6s^2$	HGH
Tl	81	[Xe] $4f^{14} 5d^{10} 6s^2 6p^1$	$5d^{10} 6s^2 6p^1$	HGH
Pb	82	[Xe] $4f^{14} 5d^{10} 6s^2 6p^2$	$5d^{10} 6s^2 6p^2$	TM

Supplementary Table S5: **Norm-conserving pseudopotentials used for the *GW* computations.** The pseudopotentials were generated following two different schemes: Troullier-Martins (TM)[64] and Hartwigsen-Goedecker-Hutter (HGH).[65] All TM pseudopotentials are from `http://www.abinit.org/downloads/psp-links/psp-links/lda\_tm` with the exception of Sn which was generated by FHIP98 (`http://th.fhi-berlin.mpg.de/th/fhi98md/fhi98PP/`). The HGH pseudopotentials are from `http://people.web.psi.ch/krack/potentials.html`

Supplementary Note 1: $A_2Sn_2O_3$ band gaps and effective mass for A=Li, Na, K, Rb, Cs

In the ICSD, both $K_2Sn_2O_3$ and $Rb_2Sn_2O_3$ form in the bcc structure while $K_2Sn_2O_3$ also forms in the rhombohedral structure. As both those structures show exceptionally low effective masses but band gaps slightly too low, we studied the effect of the nature of the alkali on the band gap and effective masses in both bcc and rhombohedral structure. Figure S21 shows the dependence of the band gap with the alkali for both bcc and rhombohedral structures. Both structures have an opposite behavior as going to larger alkali leads to larger gaps in bcc and to lower gaps in the rhombohedral. The GGA gaps will be underestimated but we are interested here in trends and how the band gap changes with the nature of the alkali.

For the bcc structure, the curve plateaus for K, Rb and Cs and not much increase in gap can be gained by going to larger alkali than K. In the rhombohedral case, a significant increase of the gap can be achieved by going from K to Na or Li. However, looking at stability data (i.e., decomposition of the phase in other competing compounds), we observe that the Li phase is strongly unstable (>200 meV/atom) and very unlikely to be ever formed. The Na phase however gives reasonable stability and a larger gap than K. The average hole effective mass tensor of the $Na_2Sn_2O_3$ rhombohedral has eigenvalues slightly higher than for $K_2Sn_2O_3$ but still very attractive: m_1=0.56, m_2=0.22, m_3=0.22. For $Na_2Sn_2O_3$ rhombohedral, the GW gap is computed at 2.7 eV (while the K phase is 2.4 eV).

As the valence and conduction bands do not have any alkali character, the effect of the alkali on the gap is likely to be a volume effect where different alkali change the cell volume and therefore the overlap between orbitals. This indicates that changing the lattice parameter through epitaxy could also be a way to tune the band gap in those materials.

Supplementary Methods

The link between band structure and effective mass (m) is straightforward in the case of a single isotropic parabolic valence band as the effective mass can be obtained by the curvature of the band at the valence band maximum (VBM) ($\frac{1}{m} = \frac{\partial^2}{\partial k^2} E_{\mathrm{val}}(\boldsymbol{k}_{\mathrm{VBM}})$, with $\boldsymbol{k}_{\mathrm{VBM}}$ the electron wave vector at the VBM and E_{val} the energy of the valence band). In general though, the effective mass is a tensor property, the bands can be non-parabolic, and several bands and/or several pockets in different parts of the Brillouin zone can contribute to conductivity. All these complexities are taken into account in semi-classical Boltzmann theory.[66][49] The electrical conductivity tensor of a periodic solid with a relaxation time τ (assumed to be constant), a chemical potential μ at a temperature T is

$$\boldsymbol{\sigma}_{\alpha\beta} = -e^2\tau \sum_i \int \mathbf{v}_\alpha(i,\mathbf{k})\mathbf{v}_\beta(i,\mathbf{k}) \frac{\partial}{\partial E} f(E(i,\mathbf{k}),\mu,T)\frac{d\mathbf{k}}{4\pi^3} \tag{S1}$$

Where $E(i,\mathbf{k})$ is the energy of the ith band at the $\mathbf{k}$-point k, $\mathbf{v}_\alpha(\mathbf{k}) = \frac{1}{\hbar^2}\frac{\partial}{\partial \mathbf{k}_\alpha} E(i,\mathbf{k})$ and $f(E,\mu,T)$ is the Fermi-Dirac distribution. Equation (S1) can be simplified to the following by using an integration by part

$$\boldsymbol{\sigma}_{\alpha\beta} = -e^2\tau \sum_i \int \mathbf{M}^{-1}_{\alpha\beta}(i,\mathbf{k}) f(E(i,\mathbf{k}),\mu,T)\frac{d\mathbf{k}}{4\pi^3} \tag{S2}$$

introducing $\mathbf{M}^{-\mathbf{1}}_{\alpha\beta}(i,\mathbf{k}) = \frac{\partial^2}{\partial k_\alpha \partial k_\beta} E(i,\mathbf{k})$: the effective mass tensor.

In the case of one isotropic parabolic band, the effective mass tensor is diagonal and independent of $\mathbf{k}$ ($\mathbf{M}_{\alpha\beta}(i,\mathbf{k}) = \frac{1}{m}\delta_{\alpha\beta}$) and we recover the textbook expression relating conductivity to effective mass and density of carriers n

$$\frac{\boldsymbol{\sigma_{\alpha\beta}}}{\tau} = \frac{ne^2}{m}\delta_{\alpha\beta} \tag{S3}$$

However, in the more general case the effective mass tensor can be anisotropic, depending on $\mathbf{k}$ (non-parabolic behavior), several bands can be involved and several competing pockets in different zones of the Brillouin zone can be contributing to conductivity. This is especially the case for valence bands. Therefore, to compare materials, we define in this work an average effective mass tensor $\bar{\mathbf{M}}_{\alpha\beta}$ as

$$\begin{aligned}\bar{\mathbf{M}}^{-1}_{\alpha\beta} &= \frac{\boldsymbol{\sigma}_{\boldsymbol{\alpha\beta}}}{ne^2\tau} && \text{(S4)}\\ &= \frac{-\sum\limits_i \int \mathbf{M}^{-1}_{\alpha\beta}(i,\mathbf{k}) f(E(i,\mathbf{k}),\mu,T)\frac{d\mathbf{k}}{4\pi^3}}{\sum\limits_i \int f(E(i,\mathbf{k}),\mu,T)\frac{d\mathbf{k}}{4\pi^3}} && \text{(S5)}\end{aligned}$$

This average tensor $\bar{\mathbf{M}}_{\alpha\beta}$, evaluated for a chemical potential giving the same carrier concentration (in this work 10^{18} cm^{-3}) and at the same temperature $T = 300\ K$, can be used to compare the intrinsic tendency for materials to lead to mobile charge carriers. In practice, the evaluation of the average effective mass tensor through equation (S5) requires a dense **k**-point sampling of the Brillouin zone (at least 10,000's of **k**-points per compound), and would be very time-consuming on a full database of thousands of compounds even with DFT. Instead, we have taken again a tiered screening approach where we computed the band structures along symmetry lines for each compound and evaluated a proxy to the full average effective mass tensor by computing the maximum effective mass along symmetry lines:

$$m_{\text{line}} = \max_{\alpha}\left(\frac{\sum\limits_i \int -(\frac{\partial^2}{\partial {k_\alpha}^2} E(i,\mathbf{k}_\alpha)) f(E(i,\mathbf{k}_\alpha),\mu = E_{\text{VBM}}, T = 300K)\frac{d\mathbf{k}_\alpha}{\pi}}{\sum\limits_i \int f(E(i,\mathbf{k}_\alpha),\mu = E_{\text{VBM}}, T = 300K)\frac{d\mathbf{k}_\alpha}{\pi}}\right) \qquad \text{(S6)}$$

where the maximum is among all the symmetry lines α. This approach is not as accurate as determining the exact effective mass tensor but requires much less computational time (a band structure along symmetry lines can be obtained with only a few hundred **k**-points) and can be used as a first screening before evaluating the full average effective mass tensor.

For the screening, we considered all compounds containing less than 100 atoms in the unit cell present in the Materials Project Database originally from the Inorganic Crystal Structure Database (ICSD) and containing oxygen and no elements such as rare-earths (from Z=58, Ce to Z=71, Lu), inert gases, and any element with an atomic number larger than 84 (Po).

The full tiered screening strategy, combining the line effective mass computations and full average effective mass tensor in DFT with the final GW computations on the most promising compounds, is outlined in Figure S32. Blue ovals indicate computations and red square filtering steps. From our set of 3052 binary and ternary oxides, we computed band structure for all compounds along symmetry lines using a high-throughput computational infrastructure, and DFT in the generalized gradient approximation (GGA). While bands shape are well represented by GGA, the band gap is known to be strongly underestimated in this approximation.[67] The band gap underestimation is often of at least 0.5 eV but can be as high as 2 eV.[26] As we target materials with band gaps around 3 eV to favor visible light transmission, we screen out from further consideration any compound with a GGA gap of less than 1 eV. In addition, GGA results are used to exclude materials with a (line) effective mass higher than 1.5. For the 42 compounds passing those criteria, we performed a full average effective mass tensor computation using equation (S6) and finally evaluated an accurate band gap for the most promising compounds by using *GW*.

Hashin *et al.*[68] have shown that the effective conductivity of a polycrystalline sample ($\boldsymbol{\sigma}$) constituted of uncorrelated anisotropic crystals of conductivity eigenvalues σ_1, σ_2, σ_3 (with $\sigma_1 < \sigma_2 < \sigma_3$) is bound by an upper and lower bound:

$$\sigma_1 \frac{4\sigma_1^2 + 8\sigma_1\sigma_2 + 8\sigma_1\sigma_3 + 7\sigma_2\sigma_3}{16\sigma_1^2 + 5\sigma_1\sigma_2 + 5\sigma_1\sigma_3 + \sigma_2\sigma_3} < \sigma < \sigma_3 \frac{4\sigma_3^2 + 8\sigma_3\sigma_2 + 8\sigma_1\sigma_3 + 7\sigma_2\sigma_1}{16\sigma_3^2 + 5\sigma_3\sigma_2 + 5\sigma_1\sigma_3 + \sigma_2\sigma_1} \tag{S7}$$

As $\sigma = \frac{ne^2}{m}\tau$, we can find the upper and lower bound to a resulting effective mass of a polycrystalline sample made from an anisotropic crystal of effective mass tensor eigenvalues m_1, m_2, m_3 (with $m_1 > m_2 > m_3$) (assuming a constant scattering time):

$$\frac{1}{m_1} \frac{4\frac{1}{m_1^2} + 8\frac{1}{m_1 m_2} + 8\frac{1}{m_1 m_3} + 7\frac{1}{m_2 m_3}}{16\frac{1}{m_1^2} + 5\frac{1}{m_1 m_2} + 5\frac{1}{m_1 m_3} + \frac{1}{m_2 m_3}} < \frac{1}{m} < \frac{1}{m_3} \frac{4\frac{1}{m_3^2} + 8\frac{1}{m_3 m_2} + 8\frac{1}{m_1 m_3} + 7\frac{1}{m_2 m_1}}{16\frac{1}{m_3^2} + 5\frac{1}{m_3 m_2} + 5\frac{1}{m_1 m_3} + \frac{1}{m_2 m_1}} \tag{S8}$$

So, we have:

$$m_{min} = \frac{16\frac{1}{m_3^2} + 5\frac{1}{m_3 m_2} + 5\frac{1}{m_1 m_3} + \frac{1}{m_2 m_1}}{4\frac{1}{m_3^2} + 8\frac{1}{m_3 m_2} + 8\frac{1}{m_1 m_3} + 7\frac{1}{m_2 m_1}} m_3 \tag{S9}$$

$$m_{max} = \frac{16\frac{1}{m_1^2} + 5\frac{1}{m_1 m_2} + 5\frac{1}{m_1 m_3} + \frac{1}{m_2 m_3}}{4\frac{1}{m_1^2} + 8\frac{1}{m_1 m_2} + 8\frac{1}{m_1 m_3} + 7\frac{1}{m_2 m_3}} m_1 \tag{S10}$$

Supplementary References

[60] Pellicer-Porres, J. *et al.* On the band gap of $CuAlO_2$ delafossite. *Appl. Phys. Lett.* **88**, 181904 (2006).

[61] Dekkers, M., Rijnders, G. & Blank, D. H. a. $ZnIr_2O_4$, a p-type transparent oxide semiconductor in the class of spinel zinc-d^6-transition metal oxide. *Appl. Phys. Lett.* **90**, 021903 (2007).

[62] Reynolds, D. *et al.* Valence-band ordering in ZnO. *Phys. Rev. B* **60**, 2340–2344 (1999).

[63] Reimann, K., Steube, M. & Dortmund, U. Experimental determination of the electronic band structure of SnO_2. *Solid State Commun.* **105**, 649–652 (1998).

[64] Troullier, N. & Martins, J. L. Efficient pseudopotentials for plane-wave calculations. *Phys. Rev. B* **43**, 1993 (1993).

[65] Hartwigsen, C., Goedecker, S. & Hutter, J. Relativistic separable dual-space Gaussian pseudopotentials from H to Rn. *Phys. Rev. B* **58**, 3641 (1998).

[66] Ashcroft, N. W. & Mermin, N. D. *Solid State Physics* (Brooks Cole, 1976).

[67] Sham, L. & Schlüter, M. Density-functional theory of the energy gap. *Phys. Rev. Lett.* **51**, 1888–1891 (1983).

[68] Hashin, Z. & Shtrikman, S. Conductivity of polycrystals. *Phys. Rev.* **130**, 129–133 (1963).